NMR relaxation of neritic carbonates: An integrated petrophysical and petrographical approach

Benoit Vincent [a,*], Marc Fleury [b], Yannick Santerre [b], Benjamin Brigaud [c]

[a] Cambridge Carbonates Ltd, 1 rue de Varoux 21120, Marey-sur-Tille, France
[b] IFP, 1-4 avenue de Bois Préau, 92852 Rueil-Malmaison cedex, France
[c] Université Paris Sud, UMR CNRS 8148 IDES, Bat. 504, 91405 Orsay cedex, France

ABSTRACT

A set of carbonate outcrop samples, covering a wide range of the sedimentary textures and depositional environments existing on carbonate systems, was studied through an integrated petrographical and petrophysical approach. With the aim of improving the understanding of the NMR (Nuclear Magnetic Resonance) signal of carbonates, this work is: 1) providing an atlas for various carbonate reservoir rock-types, 2) providing a workflow for integrating geological and petrophysical data and, 3) documenting common shortfalls in NMR/MICP analyses in carbonates. The petrographical investigation includes thin section and SEM (Secondary Electron Microscope) observations, whereas petrophysical investigation includes porosity (Φ), permeability (K), NMR, MICP (Mercury Injection Capillary Pressure), and specific surface area (BET) measurements.

On the basis of NMR and MICP data, 4 groups of samples were identified: (1) microporous samples, (2) micro–mesoporous samples, (3) wide multimodal samples, and (4) atypical samples. The microporous samples allow us to define a maximum NMR threshold for microporosity at a T_2 of 200 ms.

NMR and MICP response of the investigated carbonates are often comparable in terms of modal distribution (microporous, micro–mesoporous and wide multimodal samples). In particular, micritization, a well known but underestimated early diagenetic process, tends to homogenize the NMR signal of primarily different sedimentary facies. A grainstone with heavily micritized grains can display well sorted unimodal NMR and MICP signatures very similar, even identical, to a mudstone–wackestone. Their signatures are comparable to that of a simple sphere packing model.

On the contrary, several samples (labeled atypical samples) show a discrepancy between NMR and MICP response. This discrepancy is explained by the fact that MICP can be affected by the physical connectivity of the pore network, in case of disseminated and isolated molds in a micrite matrix for instance. Similarly, NMR can differentiate pore classes but with less resolution. It does not rely on connectivity but can be affected by diffusional pore coupling, i.e. the diffusion of water molecules carrying the magnetization between micropores and macropores. The pore-coupling phenomenon, through its impact on the T_2 distribution, may disturb the permeability calculations from NMR data.

For core plug characterization, NMR appears to be a complementary tool to MICP and should be used to complete rock-typing analysis in carbonates. For reservoir rock-typing, the obvious advantage of developing a NMR based approach is the use of NMR logging data providing continuous records of pore size distributions.

© 2011 Elsevier B.V. All rights reserved.

1. Introduction

The interpretation of NMR (Nuclear Magnetic Resonance) relaxation has been used extensively during the last decade for petroleum exploration. It is now becoming a classic wireline tool providing crucial information from pore-size distributions, porosity (Φ) and permeability (K) to saturation and fluid(s) mobility (e.g. Fleury, 2000; Minh et al., 1997; Nurmi and Standen, 1997; Westphal et al., 2005). In the context of well logging, NMR is the only technique providing a pore size distribution in addition to porosity and thus, it can obviously be used for reservoir rock-typing — i.e. an oil industry technique to predict the distribution of petrophysical properties in reservoirs (e.g. Akbar et al., 1995, 2001). For now, rock-typing is still mainly based on integrated interpretations of Mercury Injection Capillary Pressure (MICP), permeability (K) measurements, and petrographic observations from thin sections.

* Corresponding author. Tel.: + 33 6 45 08 40 16.
  E-mail address: benoit@cambridgecarbonates.co.uk (B. Vincent).

Despite few rock-typing oriented investigations (e.g. Allen et al., 2001; Frank et al., 2005; Skalinski et al., 2009) the richness of the NMR signal is both its strength and its weakness since it remains very difficult to determine and calculate precisely all the parameters listed previously for exploration in carbonates. Indeed, many effects such as pore coupling (e.g. Anand and Hirasaki, 2005; Toumelin et al., 2003), surface relaxivity variation with mineralogy and with temperature, and internal gradient can contribute to uncertainties with interpretation. In particular in carbonate rocks, the interpretation of NMR signals is so complex and variable (e.g. Moss, 2000) that it is often very difficult to use it in terms of rock-fabrics (sensu Lucia, 1999), hence the danger to interpret a signal without any connection to geological reality.

With the aim of using NMR logging data for rock typing, one of the objectives in this laboratory study is to explain the NMR signal in terms of geological observations from petrography and SEM, and compare the NMR and MICP pore and throat size distributions in carbonate samples. This paper presents a petrographical and petrophysical study of plug samples from a variety of carbonate outcrop covering a wide range of (1) the sedimentary textures and depositional environments observed in carbonate platform systems, in particular ramp setting, and consequently in carbonate reservoirs, and (2) their petrophysical properties (porosity Φ and K). The objective is to find a relationship between petrographical and petrophysical information with the aim of better defining the geological attributes that control the NMR response. In particular the process of early diagenetic (eogenesis) alteration of the primary sedimentary facies appears to be a crucial factor in understanding the rock-fabric properties (e.g. Kenter et al., 2002; Melim et al., 2001) and the NMR signal of some carbonates.

The primary objective is to bridge the gap in understanding between geologists and petrophysicists by highlighting the non-uniqueness of petrophysical properties in carbonates through an illustration of typical examples from a carbonate ramp system (Paris Basin).

2. Methods and techniques

2.1. Sample selection

To perform this work, cubic decimeter size blocs of rock samples were collected for all the investigation techniques from outcrops where rocks are assumed to be petrophysical analogs of subsurface reservoir rocks, thus displaying good visual estimates of porosity and permeability. The processes that are responsible for the current reservoir properties is not of main interest here (even if it most probably occurred during telogenesis sensu Choquette and Pray, 1972) since the focus is on petrophysical and geological attributes of the present rocks. The dataset covers a wide range of petrographical textures (Table 1), from fine microcrystalline carbonates (mudstone) to coarse grained carbonates (grainstone), and so, consequently, a wide range of the depositional environments existing on carbonate systems, in this particular data set a carbonate ramp in the Paris Basin (Table 1; Fig. 1). All 16 samples were collected from Mesozoic (Dogger, i.e. Mid Jurassic, and Malm, i.e. Upper Jurassic) and Cenozoic formations of France (Paris Basin and South East France).

In practice, the cubic decimeter size blocs were collected on freshly weathered outcrops to allow repetitive plugging in the laboratory using a hollow drill bit to extract plugs of 15 to 40 mm in diameter. Petrophysical and geological analyses were performed on the same plug whenever possible, or at least on nearby companion plugs, to avoid uncertainties linked to local heterogeneities. The homogeneity of each plug was verified using a medical X-ray CT scanner. Representativeness – homogeneity – with respect to the parent plug sample of miniplugs (~5 mm diameter) for BET (Brunauer, Emett and

Teller method; Brunauer et al., 1938) analyses and NMR measurements were carefully verified prior to drilling.

2.2. Analytical protocol

2.2.1. Petrographic observations

Geological attributes like texture, fabric, grain types, pore types, mineralogy, indicators for cementation and dissolution, etc., were analyzed through petrographic observations using standard thin sections (30 μm thick) impregnated with blue stained epoxy to indentify the pore space. The latter has then been described following the classification (Table 1) by Choquette and Pray (1970), and Lønøy (2006). The classification by Dunham (1962) and Folk (1959) were used to describe the texture of the samples (Table 1).

Thin sections were partially stained with Alizarin red S + potassium ferricyanide solution (Lindholm and Finkelman, 1972) to identify the mineralogy present in the samples (calcite vs. dolomite). A particular attention was paid to avoid samples with iron oxi-hydroxides since NMR signal is highly sensitive to such minerals.

Both polished and freshly broken pieces of samples were also observed under SEM (Scanning Electron Microscope), to identify the microporosity (here the range of pore sizes below the resolution of the thin section which is typically ~30 μm) present in the matrix of the finest facies and in some micritic components of the grainy facies.

A high resolution X ray CT-scanner was used on samples of 15 mm to complement the classical petrographic observations on thin sections with a quantitative 3D image showing small scale variation in porosity below the 3 micron lower resolution limit and pores above this limit.

2.2.2. Porosity (Φ) and permeability (K) measurements

Φ and K were measured on each sample. Porosity was determined with helium (Table 1) and by NMR after saturation. These two values were in good agreement. Water permeabilities were determined using a Hassler cell (Table 1).

2.2.3. Mercury Injection Capillary Pressure (MICP)

In a mercury injection experiment, one measures the volume of mercury penetrating the porous media for a given pressure increment (see textbooks such as Dullien, 1992). From the derivative of that curve, the pore-throat distribution $f(d_{HG})$ is obtained according to:

$$f(d_{HG}) = \frac{P^2}{2\gamma \cos\vartheta} \frac{dS}{dP} \tag{1}$$

where P is pressure, S saturation, γ surface tension and ϑ contact angle. Here, the function is a true distribution in the mathematical sense. However, it is well known that f is not the appropriate way for representing the throat size distribution (Lenormand, 2003). It is therefore recommended to plot instead the dimensionless function g defined by the following equation in order to retrieve the usual aspect of MICP derived distribution:

$$g(d_{HG}) = P \frac{dS}{dP}. \tag{2}$$

The derivative is calculated using spline fitting of the S(P) curve.

The MICP derived distribution only reflects the volume accessible through the throats at a given pressure. If the connectivity of the porous structure is such that large pores are accessible only through small throats, the measured distribution will not reflect the actual structure of the media analyzed. This will be illustrated by one example in this work.

Table 1
Geological description (texture, depositional environments, rock-fabric classes according to various classifications) and petrophysical measurements for the 16 samples used in this work.

Samples	Age	Location	Texture (Dunham, 1962)	Texture (Folk, 1959)	Depositional environment (Burchette and Wright, 1992)	Sample groups (this work)	K (mD)	Porosity (%)	BET surface (m²/g)
EST (1)	Burdigalian (Miocene)	SE France	Red algae rich grainstone	Biosparite	Agitated mid ramp	Wide multimodal	175.00	31.90	0.52
ESP (322)	Burdigalian (Miocene)	SE France	Bioclastic grainstone	Biosparite	Agitated distal inner ramp	Wide multimodal	600.00	28.59	1.83
EUV (413)	Middle Oxfordian (Malm)	NE Paris Basin	Crinoidal grainstone	Biosparite	Agitated distal inner ramp	Wide multimodal	300.00	18.68	
EUV-HAU	Middle Oxfordian (Malm)	NE Paris Basin	Crinoidal grainstone	Biosparite	Agitated distal inner ramp	Wide multimodal	3.00	13.08	0.10
EUV	Middle Oxfordian (Malm)	NE Paris Basin	Crinoidal grainstone	Biosparite	Agitated distal inner ramp	Wide multimodal	300.00	15.38	0.13
BR1	Lutetian (Eocene)	Central Paris Basin	Miliolid rich grainstone	Biosparite	Shoal in inner ramp	Atypical	2150.00	42.60	1.19
BR2	Lutetian (Eocene)	Central Paris Basin	Miliolid rich grainstone	Biosparite	Shoal in inner ramp	Atypical	2350.00	38.10	
BR3	Lutetian (Eocene)	Central Paris Basin	Miliolid rich grainstone	Biosparite	Shoal in inner ramp	Atypical	730.00	39.35	
LAV (2451)	Bathonian (Dogger)	SW Paris Basin	Ooid rich grainstone	Oosparite	Agitated distal inner ramp	Atypical	19.00	24.36	0.73
LAVF (82)	Bathonian (Dogger)	SW Paris Basin	Fine ooid rich grainstone with internal sediment	Oosparite/micrite	± quiet inner ramp	Atypical	6.00	26.33	0.69
CHA	Bathonian (Dogger)	SE Paris Basin	Dolomitized oolithic grainstone with internal sediment	Dolomitized oosparite/micrite	Oolithic shoal in internal ramp	Atypical	0.20	17.45	1.05
HAU	Middle Oxfordian (Malm)	NE Paris Basin	Oobioclastic grainstone	Oobiosparite	Agitated distal inner ramp	Micro–mesoporous	0.80	16.68	0.34
MAS	Bathonian (Dogger)	SE Paris Basin	Oobioclastic dolomitized packstone	Dolomitized oobiomicrite	± quiet inner ramp	Micro–mesoporous	0.70	14.75	0.71
ANS	Bathonian (Dogger)	SE Paris Basin	Oobioclastic grainstone with internal sediment	Oobiosparite/micrite	Oolithic shoal in inner ramp	Microporous	1.00	25.10	0.88
GUD	Upper Oxfordian (Malm)	NE Paris Basin	Peloid rich bioclastic wackestone/packstone	Pelbiomicrite	Quiet inner ramp, lagoon	Microporous	0.45	22.68	0.72
CRE	Middle Oxfordian (Malm)	NE Paris Basin	Bioclastic mudstone/wackestone	Biomicrite	Mid to outer ramp	Microporous	0.75	27.34	1.14

1 — Chalky micropores, uniform; 2 — chalky micropores, patchy; 3 — interparticle mesopores, uniform; 4 — interparticle macropores, uniform; 5 — moldic macropores (from Lønøy, 2006).

2.2.4. Nuclear Magnetic Resonance (NMR)

2.2.4.1. Basics. The method of NMR logging which is detailed in Dennis (1997) or Dunn et al. (2002) is not a primary topic here, however, its basic principles will be briefly described before describing more precisely the laboratory approach in this work.

In NMR experiments, the measured magnetization decay of water molecules is analyzed in order to deduce some information on the pore structure. The magnetization is due to hydrogen nuclei which possess a magnetic moment. They can be viewed as magnetic dipoles (Fig. 2) that have a random orientation in the absence of an external magnetic field (generated either by the logging or laboratory tool). The extremely small magnetization cannot be measured directly and a resonance technique must be used. For this purpose, a magnetic field B_1 is generated to tilt the magnetization in a direction perpendicular to the static magnetic field B_0 (Fig. 2). To be efficient, the B_1 field must oscillate at a precise frequency depending on the B_0 value. In the present work, measurements were performed at a frequency higher than usual (23.7 MHz vs. 2 MHz) because the small plugs cannot be analyzed with the same instrument used for standard plugs. However, this difference does not generate significant differences for carbonate rocks. Indeed, the comparison of the results at these two frequencies using companion samples from the same block showed no significant difference. This is explained by the low magnetic internal gradients present in carbonates, and by the small values of interecho times TE used in the experiments, yielding a negligible diffusion term (Eq. (4)). The B_1 field is turned on for a very short time (about 10 μs) and then stopped. The magnetization then returns to its equilibrium, i.e. the hydrogen nuclei attempt to return to their original alignment to B_0 through a precessional motion (Fig. 2), and is measured along the B_1 direction at regular time intervals. For a non viscous liquid, the magnetization decay is due to very short range magnetic interactions between dipoles (carried by water molecules); they are effective only when water molecules are very close, under the effect of molecular diffusion. For water, the magnetization decay is very slow (15 s corresponding to an exponential decay with a time constant 3 s) due to fast and random molecular motion (10^{-11} s). In the case of water-filled pore network in a solid, similar short-term interactions between water molecules and the solid surface occur but their strength is three orders of magnitude larger. Hence, due to diffusional motions in the pore space of water molecules used as probes, the solid surface is explored at a very small scale. The magnetization decay then depends primarily on the amount of solid surface and is typically decaying with a time constant of the order of 100 ms for oil bearing rocks. Two types of magnetization decay rate, or relaxation times, exist: (1) the relaxation time T_1, i.e. longitudinal relaxation time, is the time necessary for the longitudinal component of the magnetization to come back to its original value, and (2) the relaxation time T_2, i.e. transverse relaxation time, is the relaxation in a plane perpendicular to the static field B_0. In the present study, T_1 and T_2 provide the same information.

ρ_2 (µm/s)	Normalized values			Real values from MICP cut-offs			MacroΦ/ microΦ	Pore-type (Choquette and Pray, 1970)	Dominant pore-type	Main pore fabric (Lønøy, 2006)
	MacroΦ (%)	MesoΦ (%)	MicroΦ (%)	MacroΦ (%)	MesoΦ (%)	MicroΦ (%)				
5.00	56.90	15.50	27.60	17.75	4.84	8.61	2.06	Interparticle primary/secondary	Interparticle primary	4
3.50	65.00	10.50	24.50	17.23	2.78	6.49	2.65	Interparticle primary/secondary	Interparticle primary	4
	64.80	9.40	25.80	12.70	1.84	5.06	2.51	Cement reduced interparticle primary	Interparticle primary	
8.40	51.50	11.20	37.30	6.28	1.37	4.55	1.38	Cement reduced interparticle primary	Interparticle primary	4
8.00	62.60	9.50	27.90	8.33	1.26	3.71	2.24	Cement reduced interparticle primary	Interparticle primary	4
5.70	53.20	17.30	29.50	22.18	7.21	12.30	1.80	Interparticle primary	Interparticle primary	4
	56.00	13.90	30.10	20.27	5.03	10.90	1.86	Interparticle primary	Interparticle primary	4
	55.90	19.80	24.30	17.83		7.75	2.30	Interparticle primary	Interparticle primary	4
13.40	29.20	17.30	53.50	7.33	4.34	13.43	0.55	Solution enlarged interparticle primary and intraparticle microporosity	Interpart. primary + intrapart. microporosity	4
5.10	7.00	30.20	62.80	1.81	7.79	16.20	0.11	Solution enlarged intraparticle microporosity	Intraparticle microporosity	3
4.50	0.00	0.00	96.30	0.00	0.00	17.43	0.00	Moldic secondary	Moldic	2
4.70	9.30	19.90	70.80	1.51	3.22	11.47	0.13	Solution enlarged intraparticle microporosity	Intraparticle microporosity	2
	11.30	63.30	25.40	1.33	7.47	3.00	0.44	Moldic secondary mesoporosity	Moldic	5
3.20	0.00	0.00	95.60	0.00	0.00	21.61	0.00	No visible	No visible	1
1.60	0.00	0.00	97.30	0.00	0.00	18.68	0.00	Solution enlarged microporosity (almost not visible)	No visible	2
3.20	0.00	0.00	99.70	0.00	0.00	24.83	0.00	No visible	No visible	1

In practice, a sample is simply saturated with brine (20 g/l NaCl) and placed in a glass tube which is inserted into the NMR apparatus. Then, the transverse magnetization decay curve M(t) is measured during a few minutes at regular time intervals 2τ (about 100 µs in this work) using a CPMG sequence. M(t) is then analyzed as a sum of exponential decays (example in Fig. 3A) such as:

$$M(t) = \sum_{i=1}^{80} A_i \exp\left(-\frac{t}{T_{2i}}\right). \qquad (3)$$
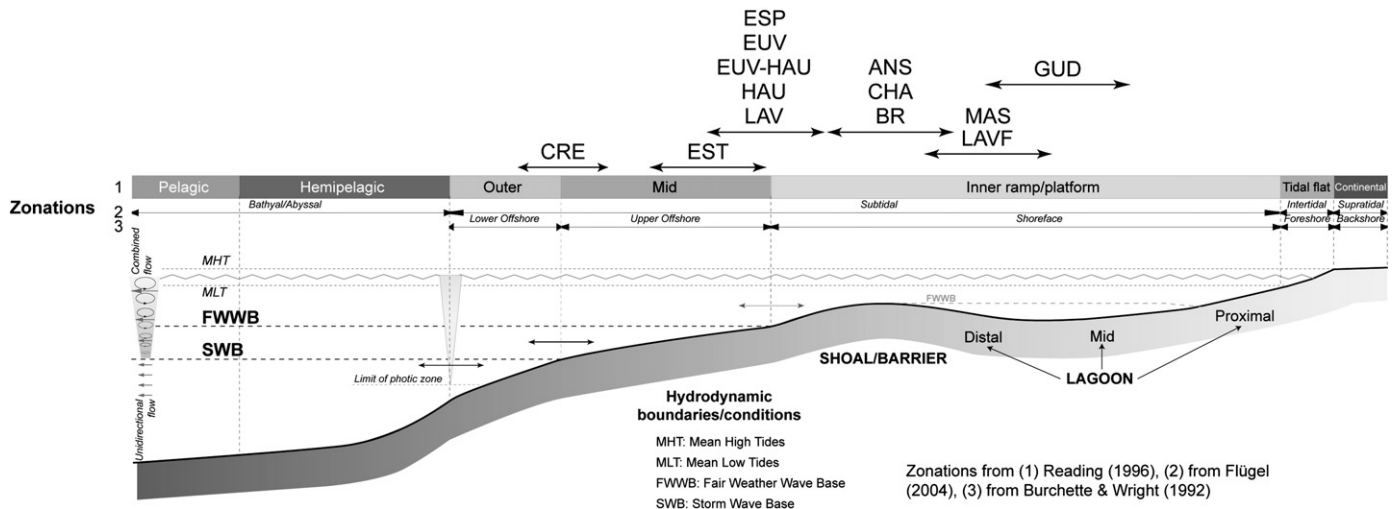

Fig. 1. Theoretical depositional profile of a carbonate platform with the various zonations used in the literature. The depositional environments of the 16 samples are projected to illustrate the range covered by the studied sample set. Zonations from (1) Reading (1996), (2) from Flügel (2004), (3) from Burchette and Wright (1992).
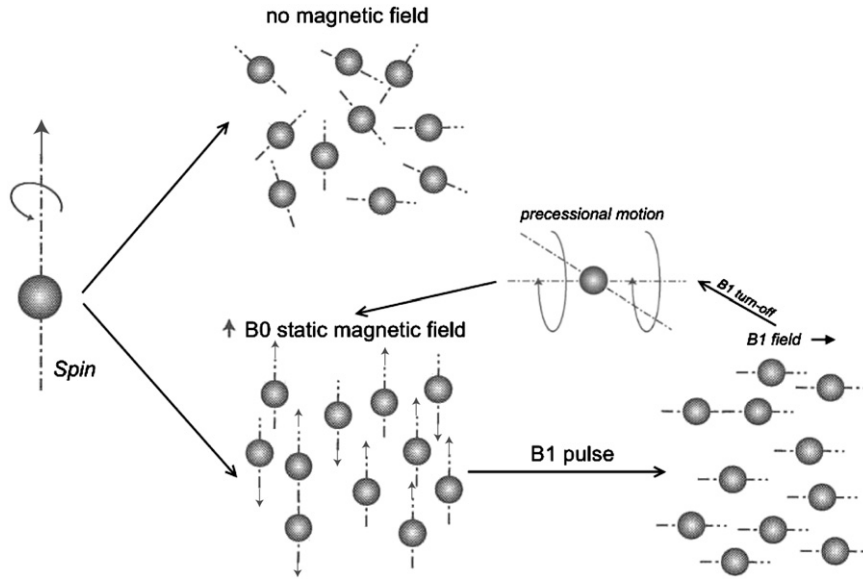
Fig. 2. Hydrogen nuclei (protons) magnetic properties (modified from Zinszner and Pellerin, 2007). Protons are assimilated to dipoles spinning around an axis, and are randomly oriented in the absence of a magnetic field. In the presence of a static magnetic field B_0 the axes line up parallel to this field, some spins being align with B_0 while others are anti-B_0. The difference between upper and lower gives the macroscopic magnetization of the material. After the B_1 pulse and turning off, the protons begin a precessional motion around the magnetic field direction to return to their original alignment along B_0. The magnetization decay, i.e. the relaxation time, is measured along the B_1 direction during this motion.

The classical plot of the amplitudes A_i as a function of T_{2i} using a logarithmic scale, called distribution of relaxation times, is obtained though a mathematical inversion process (Fig. 3B). Each T_2 component is linked to the volume to surface ratio of a compartment of the porous media according to:

$$\frac{1}{T_1} = \frac{1}{T_{1B}} + \rho_1 \frac{S}{V}$$
$$\frac{1}{T_2} = \frac{1}{T_{2B}} + \rho_2 \frac{S}{V} + \frac{1}{12}(TE\gamma G)^2 D \qquad (4)$$

where V and S are respectively the volume and surface of the compartment, T_{2B} is the bulk relaxation time of the saturating fluid (about 2700 ms for water at 30 °C), ρ_1 and ρ_2 are the surface relaxivity characterizing the strength of the solid interactions for the longitudinal and transverse relaxation, D is the molecular diffusion, γ is the gyromagnetic ratio of the proton, G is the effective magnetic field gradient across the pore, and TE is the inter-echo time of the CPMG sequence. The diffusion term involving the magnetic gradient is usually neglected, as discussed above.

The T_2 distribution is often called pore size distribution but actually reflects a distribution of V/S ratio which includes a shape factor as well as rugosity. With this in mind, it is of interest to recall some basic properties of sphere packing in terms of pore entry size and pore body size (Table 2). For these model systems, it is clearly seen that the V/S ratio of a pore is smaller than the pore-throat diameter noted d_{HG} (about a factor of 3). The latter has been calculated as the largest cylinder fitting into the pore entry and should be close to the value measured by mercury injection. However, as expected, the largest sphere fitting into the pore body is larger than the associated pore-throat. Note also that the V/S will decrease further if surface rugosity is added.

2.2.4.2. Details of the method. The primary interest when using NMR data as a tool for characterizing porous media, is the distribution of V/S deduced from the T_2 distribution. From Eq. (4), the upper limit for the detection of large pores (large values of V/S) is given by the bulk value T_{2B}, as shown in Fig. 4, using a typical value of $\rho_2 = 2$ μm/s. To correct the non linear part of the T_2–V/S relationship, the T_2 distribution is calculated using the corrected magnetization according to:

$$M(t) / \exp\left(-\frac{t}{T_{2B}}\right) = \sum_{i=1}^{80} A_{Ci} \exp\left(-\frac{t}{T_{2i}}\right). \qquad (5)$$

This calculation is more convenient than using directly Eq. (4) and subtracting T_{2B}. All the distributions shown in this work are corrected for the bulk relaxation time and are plotted up to 5000 ms. Above that value, the calculated amplitudes cannot be interpreted and reflect only the presence of very large pores.

In addition, for these large pores, the fast diffusion regime condition may not be verified (see Godefroy et al., 2001) and a determination of V/S is not possible. However, the porosity fraction associated with this pore class can still be determined. Hence, this is not critical for the present analysis.

A key assumption in the calculation of the NMR pore size distribution is that the molecules exploring the solid surface by diffusion of one compartment of the pore space are not mixed with other molecules from nearby compartments. If this mixing is occurring, there is a pore coupling effect. A clear description and modeling of this effect has been proposed recently by Anand and Hirasaki (2005), Fleury and Soualem (2009) and Toumelin et al. (2003), and a few geological examples have also been described previously by Allen et al. (2001). Fig. 5 illustrates a qualitative explanation of the NMR response in the case of pore coupling. In a theoretical two porosity system with two interparticle pore sizes $V_1/S_1 = r_1$ and $V_2/S_2 = r_2$, as a result of two different grain sizes, without coupling the NMR responses will be two peaks (Fig. 5) of amplitude N_1V_1 and N_2V_2, where N_1 and N_2 are the number of pores in each zone. The NMR response for a totally coupled system will be:

$$T_2 \propto \frac{V_T}{S_T} = \frac{(N_1 / N_2)r_1^3 + r_2^3}{(N_1 / N_2)r_1^2 + r_2^2}. \qquad (6)$$

In this case, molecules explore by diffusion the entire pore space during the magnetization decay and therefore, the total volume V_T and surface S_T must be considered. Because the microporosity contains much more surface area, the resulting measured T_2 should
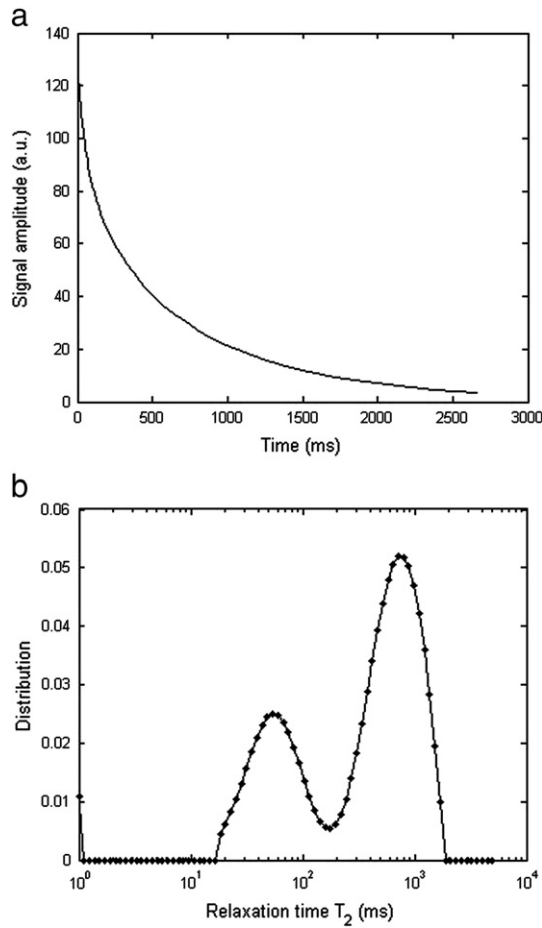
Fig. 3. Signal decay and T_2 distribution (example of measurement on the EST sample). The transverse magnetization decay curve (a) is the sum of all the decaying signals generated by protons in the sample (measurement interval of about 100 μs in this work). A mathematical inversion process allows building the more familiar T_2 distribution curve (b). The curve reflects a distribution of pore V/S ratios.

be shifted to a value close to the microporosity peak that would be measured in the absence of coupling. For example, choosing $\Phi_1 = \Phi_2$ and $r_2 = 10r_1$, then $N_1/N_2 = 10^3$ and the T_2 peak is located at $1.81r_1$, close to the microporosity peak located at $V_1/S_1 = r_1$. In general, a coupling coefficient depending on diffusivity, surface relaxivity, and geometry can be defined (Anand and Hirasaki, 2005).

2.2.5. Specific surface area

The specific surface area has been measured using the standard BET method (Brunauer et al., 1938). Identical samples (diameter 5 mm, length 5 mm) were used for both NMR and BET to avoid potential heterogeneity effects. The method uses the condensation of a gas at the solid surface, and given the surface occupied by one adsorbed molecule, the solid surface can be obtained. Due to the low specific surface area of the studied sample (smaller than about 1 m²/g) a large molecule (krypton) was used. BET is essentially used to calculate NMR surface

Table 2
Geometrical properties of sphere packs of diameter d; d_p is the pore body size (as measured by NMR, or V/S ratio, see the text), and d_{HG} is the diameter of the largest cylinder fitting into the pore throat (as measured by MICP).

Sphere pack type	Porosity	Pore entry size d_{HG}	NMR pore size $d_p = V/S$	d_p/d_{HG}	Largest sphere in pore
Cubic	0.476	0.414 d	0.151 d	0.365	0.732 d
Rhomboedric	0.259	0.154 d	0.058 d	0.377	0.224 d
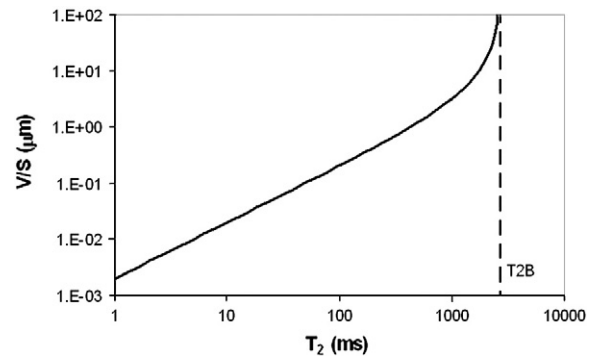
Fig. 4. Relation between V/S and a measured T_2 component of the relaxation time distribution ($\rho_2 = 2$ μm/s) from Eq. (4). Note the non linearity above 1000 ms (Fleury et al., 2007). It can be corrected using an appropriate processing, see Eq. (5).
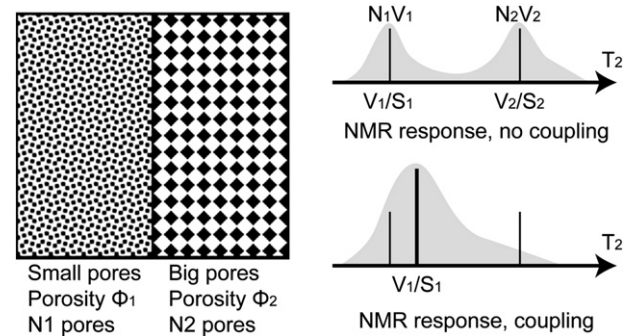
Fig. 5. Compared schematic NMR responses in the case of diffusional coupling or no coupling between two porosity zones with two different pore sizes (Fleury et al., 2007).

relaxivity as explained below. Implicitly, the surface explored by NMR and BET is assumed to be the same.

The surface relaxivity ρ_2 was estimated by first calculating an average relaxation time defined by:

$$\frac{1}{T_{2mS}} = \left(-\frac{1}{M}\frac{\partial M}{\partial t} \right)_{t=0} \cong \rho_2 \frac{S_T}{V_T} \tag{7}$$

where T_{2mS} is the average relaxation time of the T_2 distribution that reflects the ratio of total surface S_T to total volume V_T.

Table 3
Non exhaustive review of the different values of pore throat size and/or pore size boundaries available in the literature to identify micropores, mesopores and macropores in carbonates.

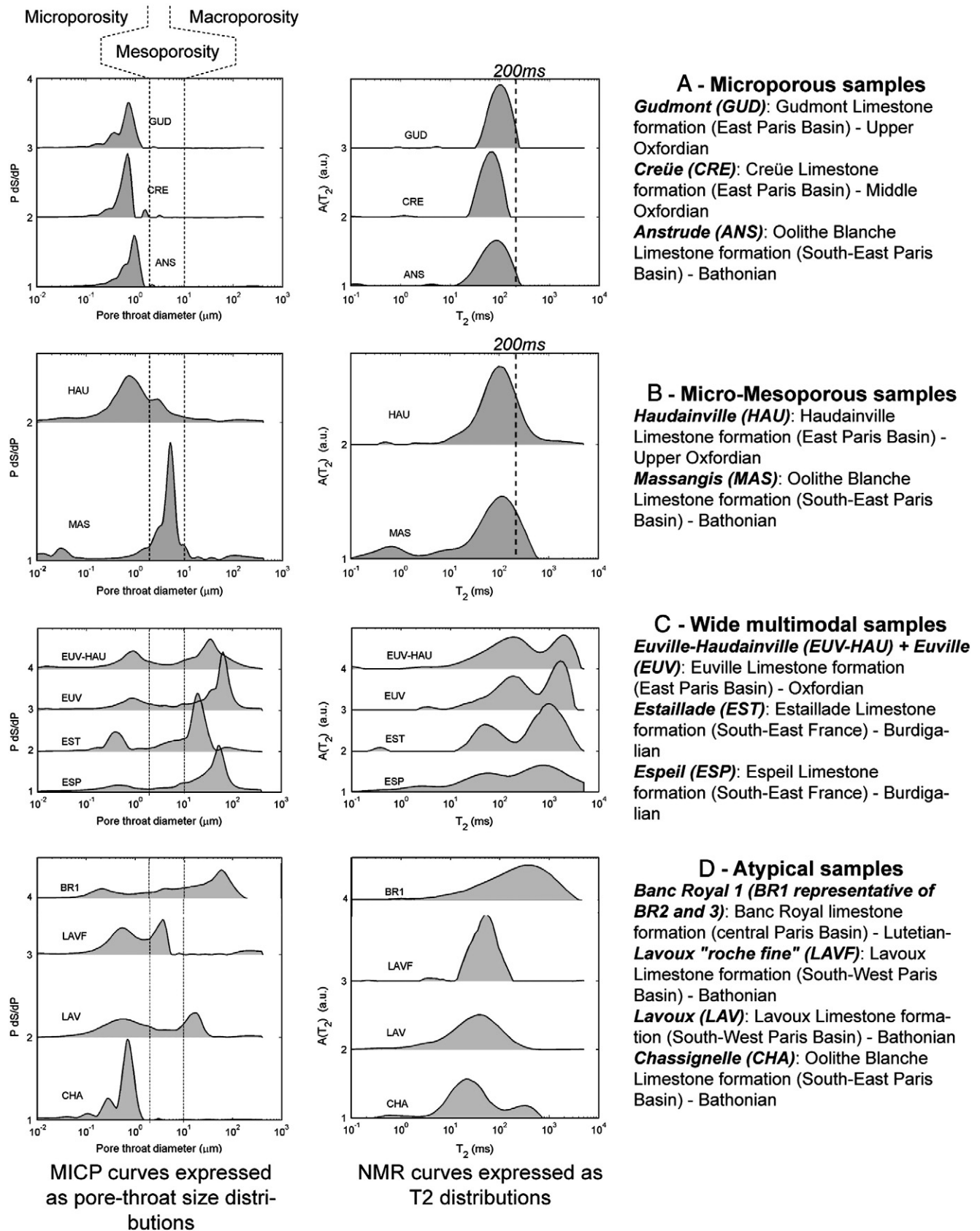| Micropores (dμm)	Mesopores (dμm)	Macropores (dμm)	Author(s)	Method	
<0.06	0.06<d<15	>15	Goni et al. (1968)	MICP	Pore-throat diameter
<0.02	0.02<d<2	>2	Bousquie (1979)	MICP	
<0.5	0.5<d<5	>5	Frank et al. (2005)	MICP	
<0.3	0.3<d<3	>3	Skalinski et al. (2009)	MICP	
<0.02	Undefined	>0.02	Combarnous and Marle (1965)	MICP	
<62.5	62.5<d<4000	>4000	Choquette and Pray (1970)	Thin sections	Pore diameter
<1	Undefined	>1	Pittman (1971)	SEM	
<10		>10	Bousquie (1979)	Thin sections	

A - Microporous samples
Gudmont (GUD): Gudmont Limestone formation (East Paris Basin) - Upper Oxfordian
Creüe (CRE): Creüe Limestone formation (East Paris Basin) - Middle Oxfordian
Anstrude (ANS): Oolithe Blanche Limestone formation (South-East Paris Basin) - Bathonian

B - Micro-Mesoporous samples
Haudainville (HAU): Haudainville Limestone formation (East Paris Basin) - Upper Oxfordian
Massangis (MAS): Oolithe Blanche Limestone formation (South-East Paris Basin) - Bathonian

C - Wide multimodal samples
Euville-Haudainville (EUV-HAU) + Euville (EUV): Euville Limestone formation (East Paris Basin) - Oxfordian
Estaillade (EST): Estaillade Limestone formation (South-East France) - Burdigalian
Espeil (ESP): Espeil Limestone formation (South-East France) - Burdigalian

D - Atypical samples
Banc Royal 1 (BR1 representative of BR2 and 3): Banc Royal limestone formation (central Paris Basin) - Lutetian-
Lavoux "roche fine" (LAVF): Lavoux Limestone formation (South-West Paris Basin) - Bathonian
Lavoux (LAV): Lavoux Limestone formation (South-West Paris Basin) - Bathonian
Chassignelle (CHA): Oolithe Blanche Limestone formation (South-East Paris Basin) - Bathonian

MICP curves expressed as pore-throat size distributions

NMR curves expressed as T2 distributions

Fig. 6. Coupled pore throat size distribution and NMR T_2 distribution for every sample arranged in 4 main groups: (A) microporous samples, (B) micro–mesoporous samples, (C) wide multimodal samples, and (D) atypical samples. Note the microporosity threshold defined by NMR T_2 at 200 ms from the microporous samples.

T_{2mS} is estimated using the first 10 measured points of the magnetization decay $M(t)$. Then, ρ_2 can be calculated with $S_T = S_{BET}$ and from the NMR pore volume V_T.

3. Sample description: a petrographical and petrophysical atlas

Generally, as part of the rock-typing workflow in carbonate reservoir characterization, MICP data are used to define cut-off values (e.g. Akbar et al., 2001). Petrographic observations (microscope or SEM) can also be used to define these cut-offs. Obviously, cut-offs defined from MICP are different from the petrographic cut-offs because of the respective resolution of investigation (Table 3). Unfortunately, it seems that each case study using MICP defines its own cut-off values and no real "universal" values may exist (Table 3).

Here, the MICP dataset (Fig. 6, left column) shows 3 main pore-size classes, interpreted as microporosity, mesoporosity, and macroporosity, respectively with pore-throat sizes smaller than 2 μm, between 2 and 10 μm, and larger than 10 μm.

Integration of MICP data with results from NMR analyses allows splitting the samples into 4 different main groups (Fleury et al., 2007; Fig. 6), without using the petrographical attributes: (1) microporous samples, (2) samples with micro and mesoporosity or mesoporosity alone, (3) wide multimodal samples (micro, meso, and/or macroporosity), and (4) atypical samples (Table 1). The latter group encompasses the samples for which NMR and MICP modal distributions show little correspondence.

In terms of simple petrophysical properties, i.e. Φ and K, this grouping appears to be coherent considering the limited sample set since the data for each group form clusters (Fig. 7), with the exception of the atypical group showing a wide range of K values (Fig. 7A). Despite the fact that these groups were defined only on the basis of MICP and NMR, there is definitely a relationship existing with the petrographic attributes, and especially with the dominant pore type characterization following the Choquette and Pray (1970) classification (Fig. 7). The wide multimodal samples display mainly primary interparticle porosity and show the highest permeability (Fig. 7), whereas the microporous samples are dominated by microporosity which is not visible in thin sections (Melim et al., 2001; Westphal et al., 2005). The micro–mesoporous samples, like the atypical samples, are not clearly related to one dominant pore type, but it appears that the least permeable samples of these sets display moldic porosity (Fig. 7; Table 1). Similar relationships do exist between the groups defined in this work and the Lønøy (2006) pore-fabrics. The wide multimodal samples are dominated by Class 4 pore-fabric, whereas microporous samples mostly display Class 1 and 2 fabrics. But more general assessments on Φ/K relationships linked to pore typing would however require an extended dataset (e.g. Melim et al., 2001) and this is not the aim of this paper.

Like most of the time for carbonate sample sets, there is no simple correlation between total porosity and permeability (Fig. 8). But as demonstrated by Melim et al. (2001), the contribution by macroporosity, here calculated and normalized from the MICP cut-off values (Table 1), determines the permeability (Fig. 8). Melzer and Budd (2008) also found a clear positive correlation (R^2 near 0.8) between the amount of macroporosity and the permeability by using the same 10 μm MICP cut-off as the one defined with the present dataset.

3.1. Microporous samples

The sample from the "Calcaire de Creüe" Formation (abbreviated CRE) from the Eastern Paris Basin is of Middle Oxfordian age. This bioclastic mudstone to wackestone (Fig. 9a), slightly argillaceous (less than 5% clays; Vincent, 2001), reflects an open marine depositional environment (some ammonites are reported in Enay and Boullier, 1981) in a mid to outer ramp setting. The primary intercrystalline microporosity is dominating in the micrite matrix (Fig. 9a and Table 1).
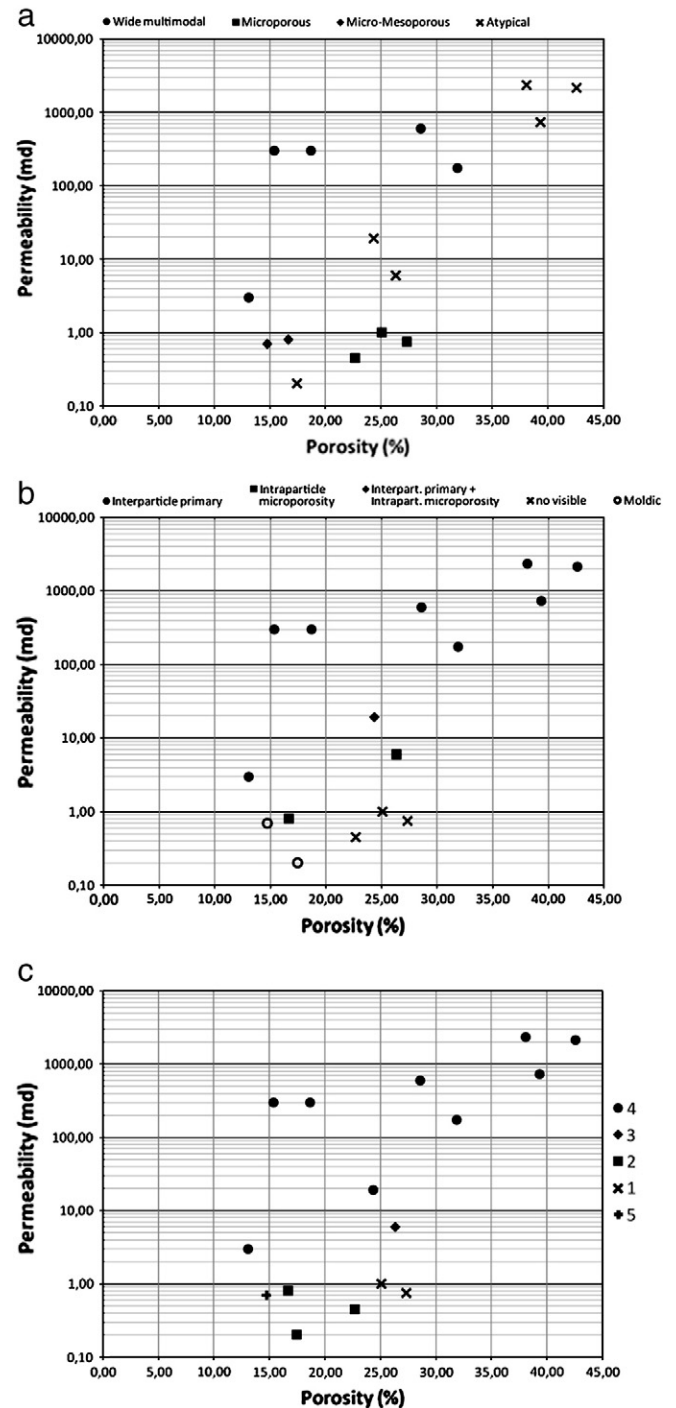

Fig. 7. Porosity/permeability cross-plot for the entire dataset. The data form clusters corresponding to the main defined groups (a), except for the atypical samples which are more scattered. The best reservoir samples are the wide multimodal samples. Samples are also plotted according to the Choquette and Pray (1970) pore-types (b), and the Lønøy (2006) pore fabrics (c).

The sample from the "Calcaire crayeux de Gudmont" Formation (abbreviated GUD) from Eastern Paris Basin is of Upper Oxfordian age. It is a heavily micritized peloid-rich bioclastic wackestone to packstone (Fig. 9b, photo A), which characterizes an inner ramp lagoon environment with low energy hydrodynamic conditions. The intercrystalline microporosity, located in the matrix (Fig. 9b, photo B; Table 1), appears to be locally altered (Fig. 9b, photo C), i.e. enlarged
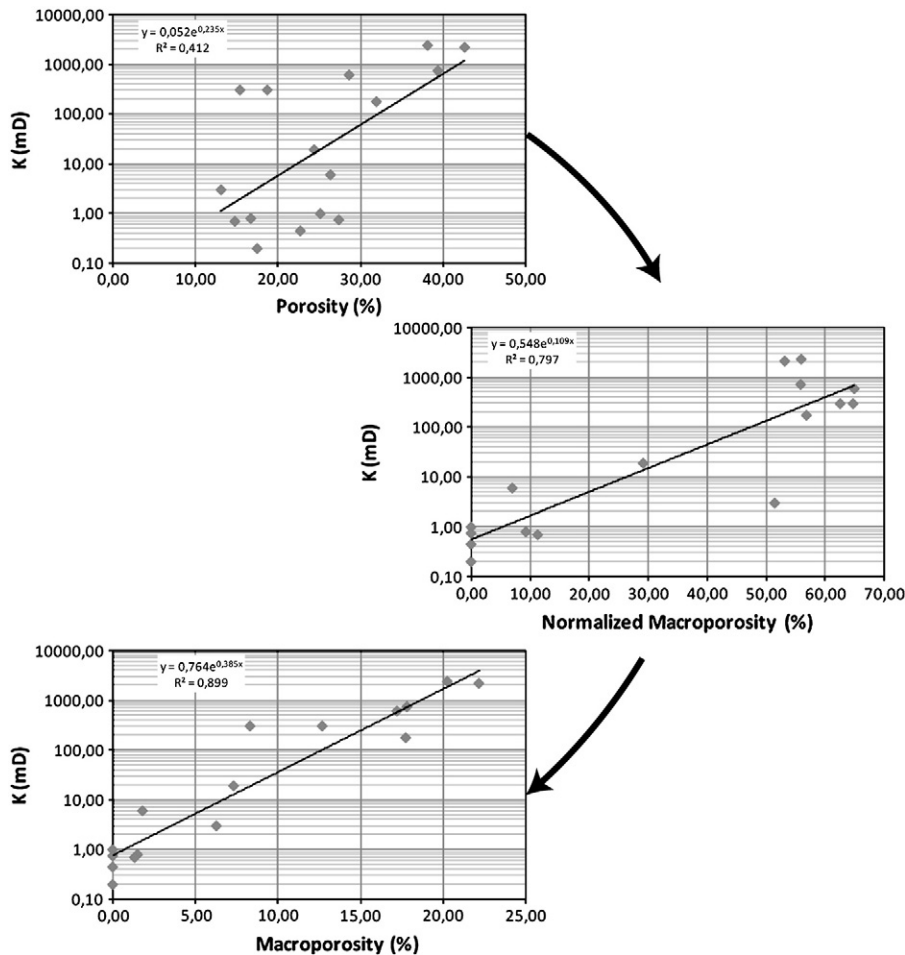
$y = 0.052e^{0.235x}$
$R^2 = 0.412$

$y = 0.548e^{0.109x}$
$R^2 = 0.797$

$y = 0.764e^{0.385x}$
$R^2 = 0.899$

Fig. 8. Porosity/permeability cross-plots. There is no good correlation between total porosity and total permeability. However, there is a good correlation between macroporosity (calculated and normalized from the MICP cut-off values) and permeability.

by dissolution as illustrated by rounded calcite crystals (e.g. Lambert et al., 2006). This alteration most probably occurred by meteoric water influx following the Tertiary uplift of the Eastern part of the Paris Basin up to present time (e.g. Vincent et al., 2007). This limestone displays a macroscopic chalky aspect.

The sample from the "Pierre d'Anstrude–Oolithe Blanche" Formation (abbreviated ANS) in the South-East Paris Basin is of Bathonian age. This oobioclastic grainstone displays extensively micritized components, contains minor detrital micrite sediment, and represents an agitated shallow marine hydrodynamic depositional environment in an inner ramp setting. The micritization of the grains (Bathurst, 1971) illustrates either (1) that the depositional environment could have been periodically quiet (tidal influence), and (2) more likely that the grains were transported outside their initial low energy depositional environment (lagoon) into this more agitated setting. The primary interparticle pore space is completely filled by an equant mosaic calcite cement (Fig. 9c), either mesogenetic or telogenetic in origin, and this sample is only microporous (Fig. 9c, photo B; Table 1).

For all these samples, no meso- or macroporosity is observed in thin sections and only microporosity is present as indicated by SEM (Fig. 9). The micropore network corresponds in each sample to the intercrystalline space between calcite crystals (Fig. 9). Despite the different sedimentological origins of these samples, and following different diagenetic evolution, both MICP and NMR response are very uniform (Figs. 6 and 9) and Φ/K values are similar (Fig. 7). MICP distributions do not extend above 2 μm, and NMR distributions not above 200 ms, both being narrow in range. All three samples also have comparable BET values (around 1 m²/g; Table 1); note also that the

lower surface relaxivity ρ_2 for the GUD sample may explain the slightly higher T_2 mode of the distribution (Fig. 6).

Noteworthy is the possibility to define a microporosity cut-off at a relaxation time T_2 of 200 ms, compared with the 2 μm pore-throat cut-off (Fig. 6).

3.2. Micro–mesoporous or mesoporous samples

The sample from the "Oolithe Blanche" Formation in the Massangis quarry (abbreviated MAS) from the South-East Paris Basin is of Bathonian age. It is an ooid dominated peloidal-bioclastic packstone, with minor echinoderm debris and small benthic foraminifers, interpreted as deposited in a low energy depositional environment of the inner ramp setting, with ooids originating from a distant and more agitated source (ooid shoals). This limestone was dolomitized (either during eogenesis or mesogenesis) and displays remnants of planar-e dolosparite (Gregg and Sibley, 1984) crystals replacing the intergranular micrite matrix (Fig. 10a). Dedolomitization, here both calcitization and dissolution, later occurred during telogenesis (i.e. late diagenesis related to recent near surface phenomena) and formed some non-perfect rhombic molds (Fig. 10a, photo B).

Since dolomite rhombs were not totally dissolved and were replaced by calcite, only mesopores are shown by MICP (Figs. 6 and 10). The NMR response is globally shifted to higher T_2 values with a wider distribution than microporous samples. However, based only on NMR data, this sample would be classified as microporous (Fig. 6).

The sample from the "Calcarénite d'Haudainville" Formation (abbreviated HAU) from the Eastern Paris Basin is of Upper Oxfordian
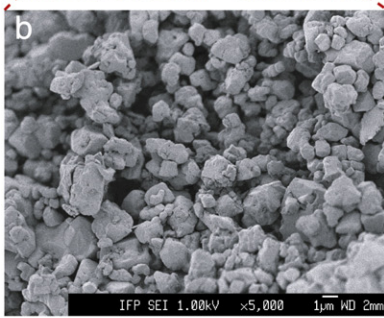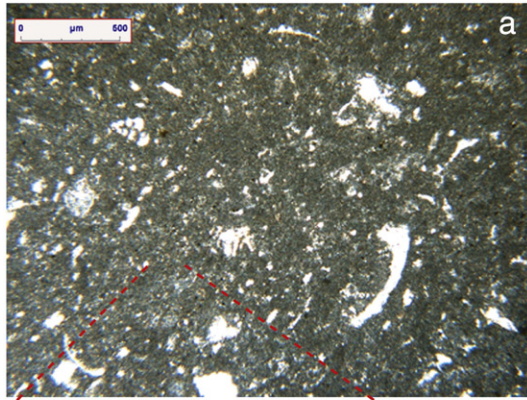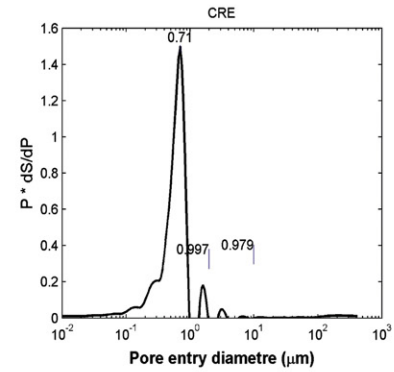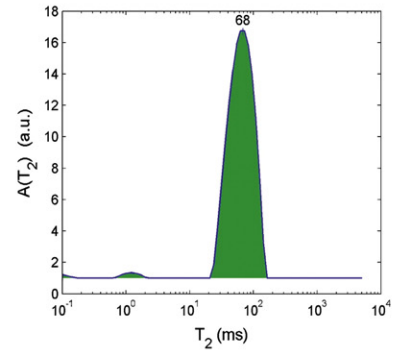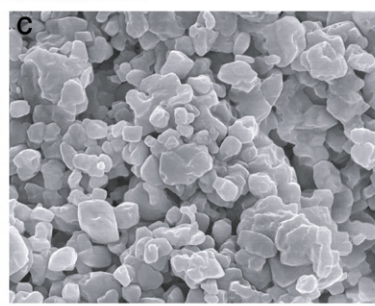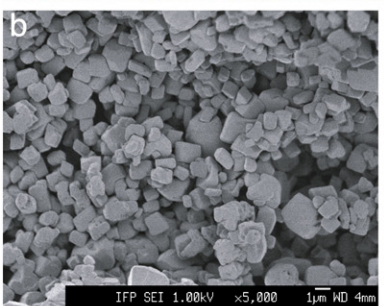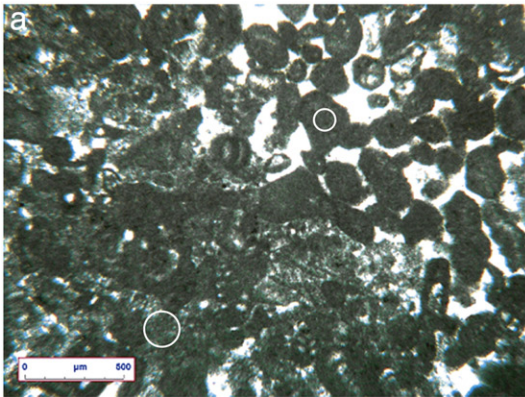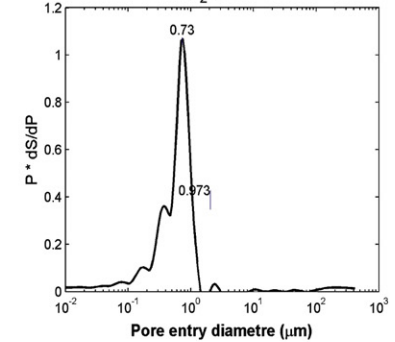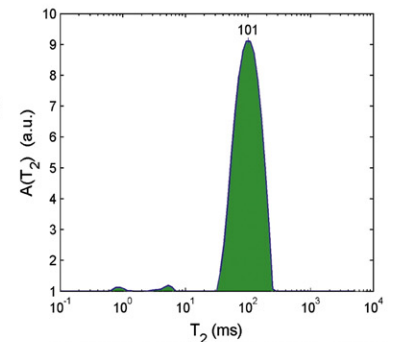
Fig. 9. Petrographical and petrophysical characteristics of the microporous samples. The micro–meso–macroporosity contributions are calculated from MICP data (this figure to Fig. 14). a) CRE sample. Photo A: PL illustration of this homogeneous bioclastic wackestone; photo B: SEM focus on the texture of the micrite matrix. b) GUD sample. Photo A: PL illustration of the micro-heterogeneity of this peloid-rich bioclastic wackestone to packstone; photo B: SEM focus on the micrite texture of the matrix and the grains (white circles on photo A); photo C: SEM focus on the locally altered texture, i.e. dissolved, of the micrite. Note the round shaped crystals and the coalescent aspect of some areas illustrating both dissolution and recrystallization. c) The ANS sample. Photo A: PL illustration of this ooid and bioclast-rich grainstone. Note the strong micritization of ooids and bioclasts (here crinoids); photo B: SEM focus on the texture of the micrite in the grains (ooid).

C
ANS Sample

Φ=25% → MacroΦ=0%
        → MicroΦ=95.6%

K=1mD
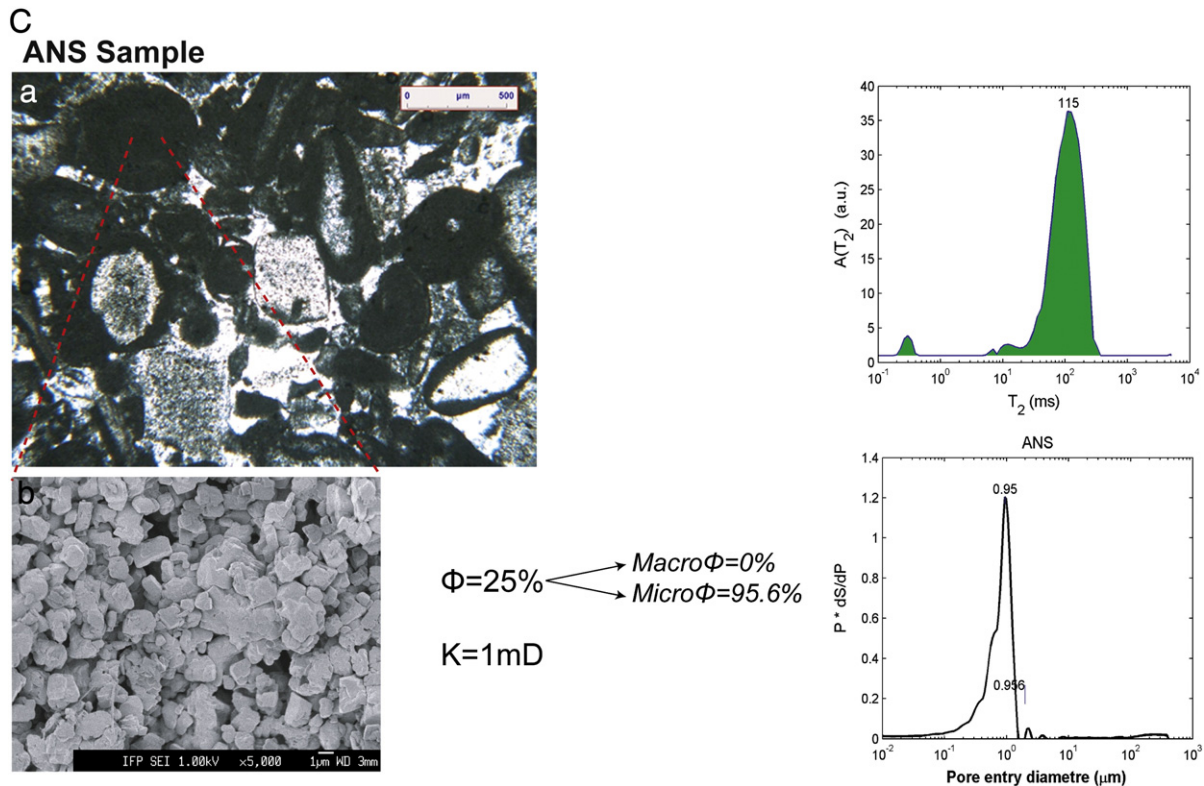
Fig. 9. (continued)

age. This coated grains-rich bioclastic grainstone reflects a relatively agitated environment in a distal inner ramp setting. Both coated grains and bioclasts are micritized, which illustrates a former low energy lagoonal origin for these detrital grains. A fibrous isopachous cement rim precipitated early after deposition leading to an early lithification of the sediment (Fig. 10b, photo A). The residual porosity was occluded during burial by an equant mosaic calcite cement (Fig. 10b, photo A).

The MICP distribution shows meso and microporosity (Figs. 6 and 10). The microporosity is located within the micrite of the external parts of grains and in the coated grain cortex (Fig. 10b, photo B), and the mesoporosity between the external laminations of the spalled ooids and/or coated grains (Fig. 10b, photos A and C). The NMR signature is very similar to MAS signature, thus a broader distribution and a shift to larger T_2 values than recorded in the microporous samples.

3.3. Wide multimodal samples

The samples from the "Pierre d'Euville" Formation (abbreviated EUV and EUV-HAU) in the Eastern Paris Basin are of Oxfordian age. This crinoidal grainstone (echinoderm debris) corresponds to an agitated depositional environment, probably in a distal inner to mid-ramp setting. Syntaxial cements precipitated as overgrowths on crinoid ossicles, and partly occluded the primary interparticle porosity (Fig. 11, photos A and B). These cements are clear, inclusion free, and therefore probably precipitated in Low Magnesian Calcite (LMC).

Minor micrite detrital sediment is visible in the remaining pores and contains microporosity (Fig. 11, photo D). Noteworthy is the microporosity of the crinoid ossicles themselves, visible in both thin sections and SEM (Fig. 11, photo C).

The sample from the "Pierre d'Estaillade" Formation (abbreviated EST) in South-East France is of Burdigalian age. It is a red algae dominated grainstone characterizing a middle ramp environment. A thin equant circumgranular to bladed cement rim precipitated around the grains early after deposition (Fig. 12, photo C). This cement is well developed and seems to maintain the integrity of the sample in some areas where the rimmed grains, probably initially aragonitic, were dissolved, either during eogenesis or telogenesis. This explains the occurrence of a large intercrystalline and/or intergranular macroporosity (Fig. 12, photos B and C).

The sample from the "Roche d'Espeil" Formation (abbreviated ESP in the following) in South-East France, is also of Burdigalian age. It is a bioclastic grainstone, rich in red algae debris but with more diversified components than EST (bivalve debris, large benthic foraminifers). This facies suggests an agitated distal inner to mid ramp depositional environment. Little remnants of an isopachous cement rim (dog tooth of bladed fabric?) and of a mosaic calcite cement are visible, because of a very important dissolution stage during telogenesis (dissolution gulf). The main pore type is an intergranular macroporosity, with also scattered molds (Fig. 12, photo A; Table 1).
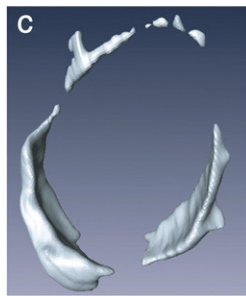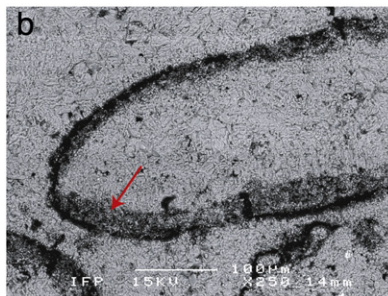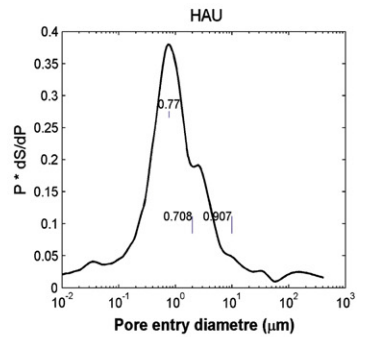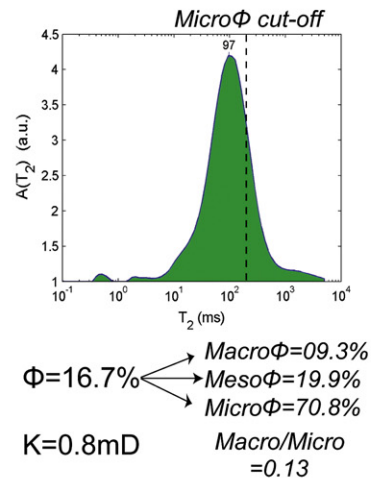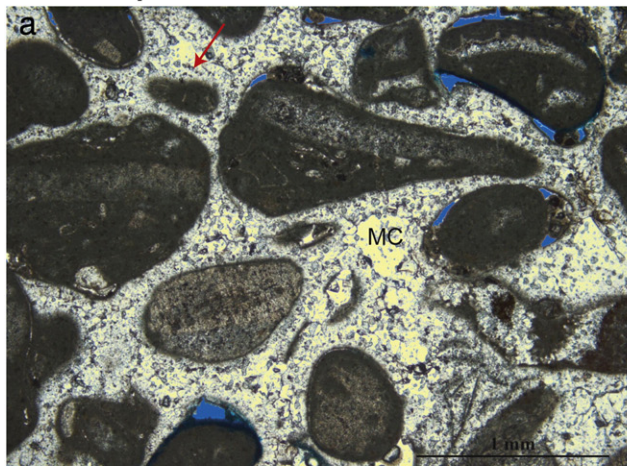
All these high permeability samples (see Table 1) have similar MICP signatures (Fig. 6): the dominant fraction of the porosity

Fig. 10. Petrographical and petrophysical characteristics of the micro–mesoporous samples. a) MAS sample. Photo A: PL illustration of this dolomitized ooid and bioclast packstone. Thin section illustrating syntaxial calcite cements (Sy) and dolomite rhomb (Dol). Note the occurrence of darker/pink dots in the dolomite rhombs; photo B: backscattered SEM illustration of a polished epoxy impregnated sample. In the rhombic areas (arrow), the black zones correspond to epoxy, thus voids, the dark gray zones are dolomite spots, and the light gray zones are calcite spots, corresponding to the grains and cements around the rhomb. This complexity illustrates that dolomite is both calcitized (non perfect calcitization) and dissolved. b) HAU sample. Photo A: PL illustration of this ooid and bioclast grainstone. An early isopachous cement rim surrounds the grains (arrow); photo B: backscattered SEM illustration of a polished epoxy impregnated sample. The black thin zone around the grain corresponds to epoxy and thus void. Note also the occurrence around the grain of a larger altered micritized and microporous zone where epoxy percolated; photo C: CT-scanner reconstruction of a pore lining an ooid (image width = 1 mm).
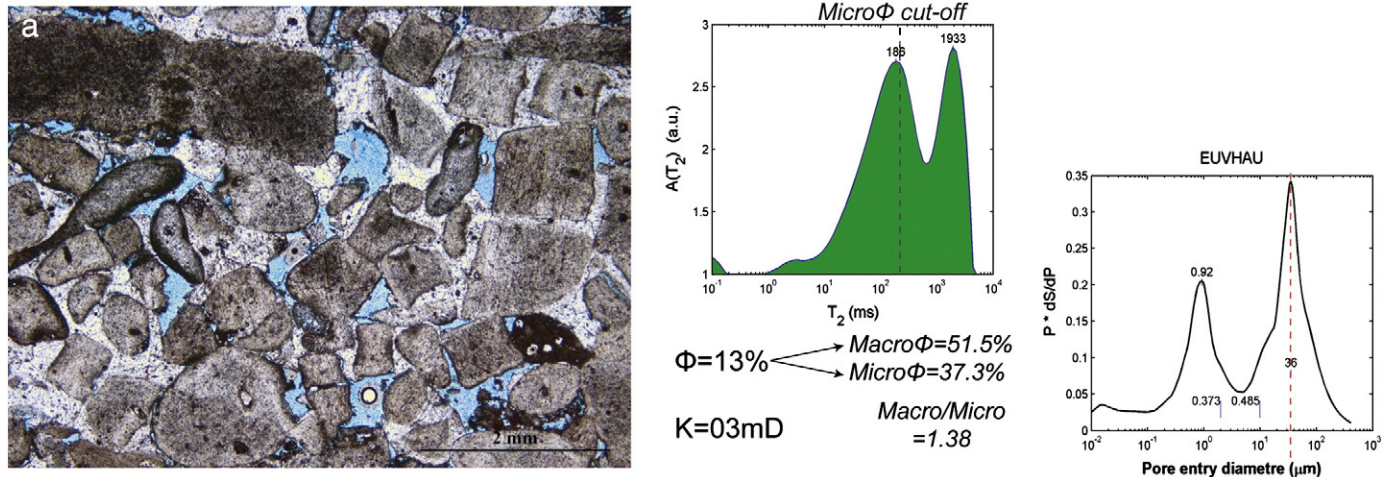
A
MAS Sample

$\Phi=14.7\%$
→ $Macro\Phi=11.3\%$
→ $Meso\Phi=63.3\%$
→ $Micro\Phi=25.4\%$

$K=0.7mD$ $Macro/Micro=0.44$

B
HAU Sample

$\Phi=16.7\%$
→ $Macro\Phi=09.3\%$
→ $Meso\Phi=19.9\%$
→ $Micro\Phi=70.8\%$

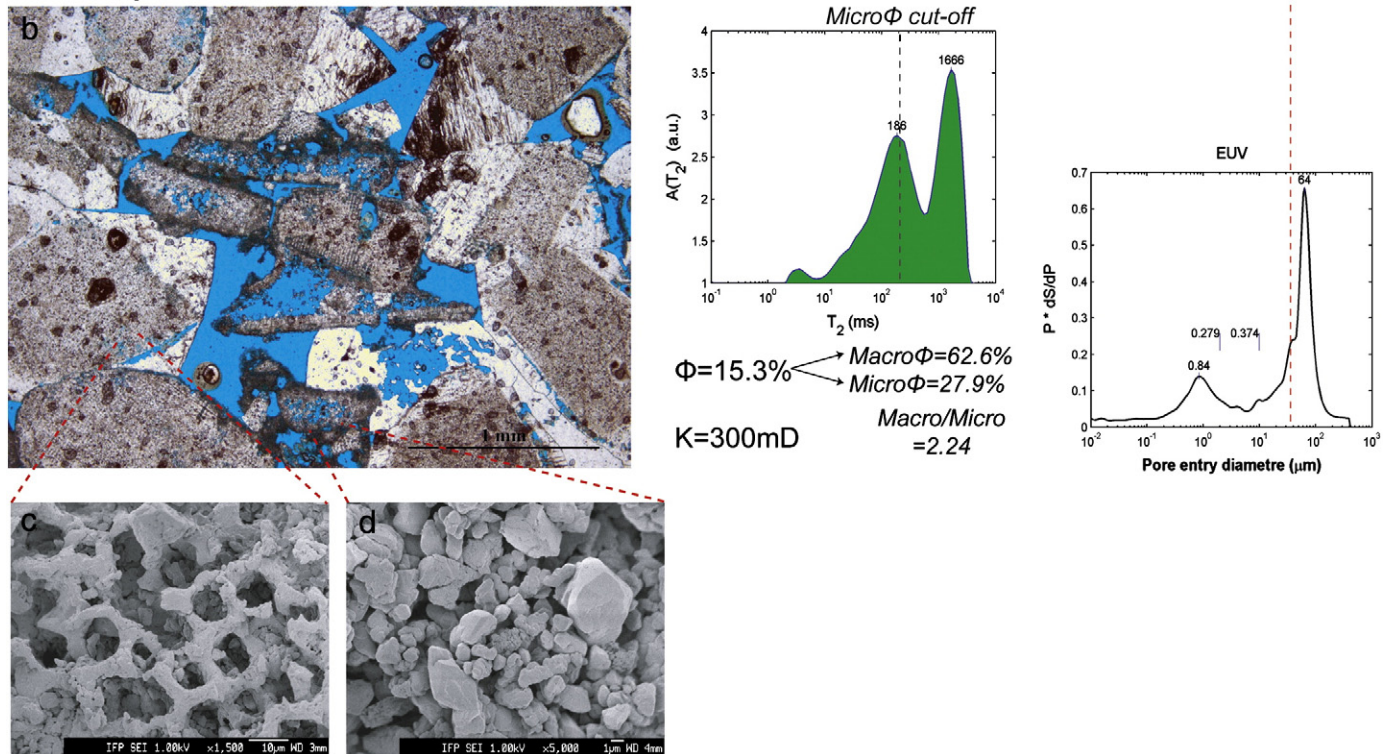$K=0.8mD$ $Macro/Micro=0.13$
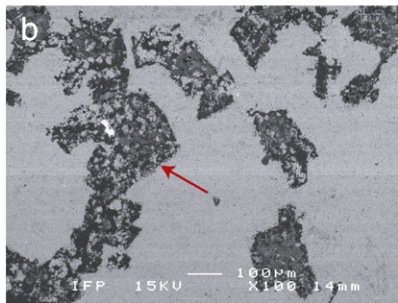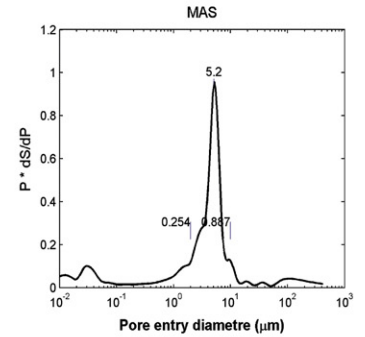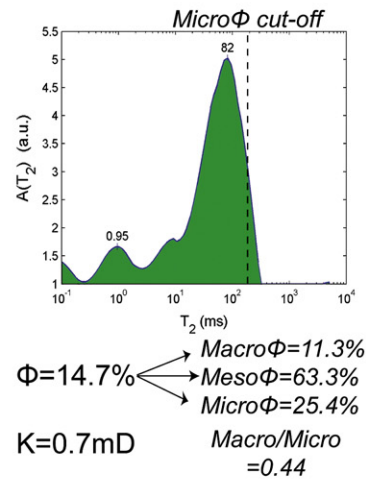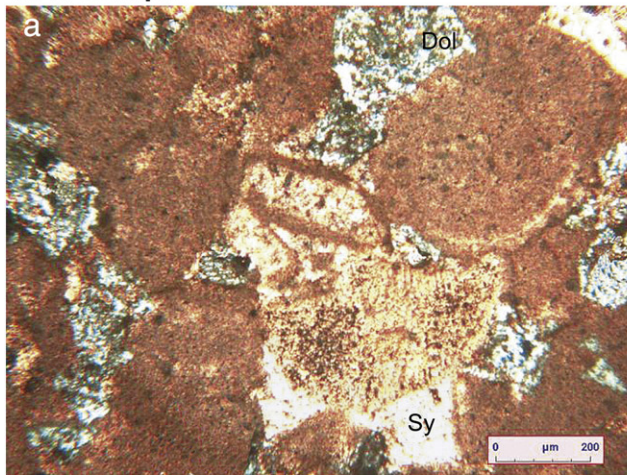
EUV-HAU Sample

EUV Sample

Fig. 11. Petrographical and petrophysical characteristics of the wide multimodal EUV-HAU and EUV samples. Photo A: PL illustration of the EUV-HAU crinoidal grainstone. Noteworthy is the abundant syntaxial overgrowths on the crinoid debris, with the occurrence of patchy cemented areas; photo B: PL illustration of the EUV crinoidal grainstone. The syntaxial cements are less developed than in EUV-HAU sample; a limiting factor being the occurrence of partially micritized and dissolved bioclasts such as bivalve debris (center of the photo). Note the dissolution of both syntaxial overgrowths and crinoid debris (homogeneous gray zones correspond to blue epoxy); photo C: SEM focus on the intra-crinoid typical pore network; photo D: SEM focus on the micrite texture on the border of micritized bioclasts. For both samples, the NMR T_2 mode of the microporosity is close to the 200 ms threshold defined by microporous samples (see further discussion in the text).

corresponds to macroporosity (Table 1; Fig. 6), and a significant fraction of the porosity corresponds to microporosity, and to a lesser degree to mesoporosity (Table 1; Fig. 6). Based on the NMR data, these samples also have a broad bimodal T_2 distribution.

For EST and ESP samples, the microporosity located in the red algae debris (Fig. 12), observed through the faint blue stain of these clasts in thin sections (Fig. 12), is clearly distinguished as a separate peak below 200 ms.

For EUV and EUV-HAU samples, the microporosity peak has a mode near 200 ms (near the 200 ms microporosity cut-off of microporous samples; Fig. 11). These high values, compared to the microporous samples (Figs. 6 and 9) cannot be explained by a lower

surface relaxivity. On the contrary, ρ_2 is slightly higher and should yield lower T_2 values (Table 1). These higher T_2 values are explained by the specific intra-crinoid microporosity which displays both larger pore size and pore-throats than the intercrystalline microporosity of the micrite matrix (Figs. 6 and 11).

The wide multimodal group displays most of the highest K values, 100 to 1000 mD, within a wide range of Φ values, 15 to 33%. An exception, however, is the EUV-HAU sample, where K is 2 orders of magnitude lower (3 mD) than the other samples of this group, despite quite similar Φ (Table 1; Fig. 7). The petrographic observation only illustrates that the syntaxial cements, overgrowing on the crinoid debris, are more developed in EUV-HAU than in EUV (Fig. 11, photos A and B).
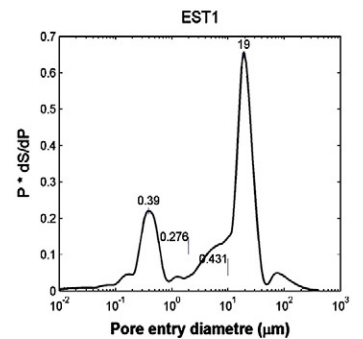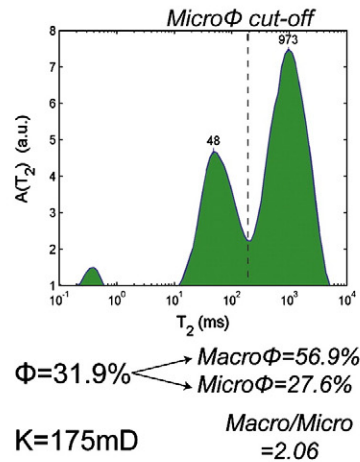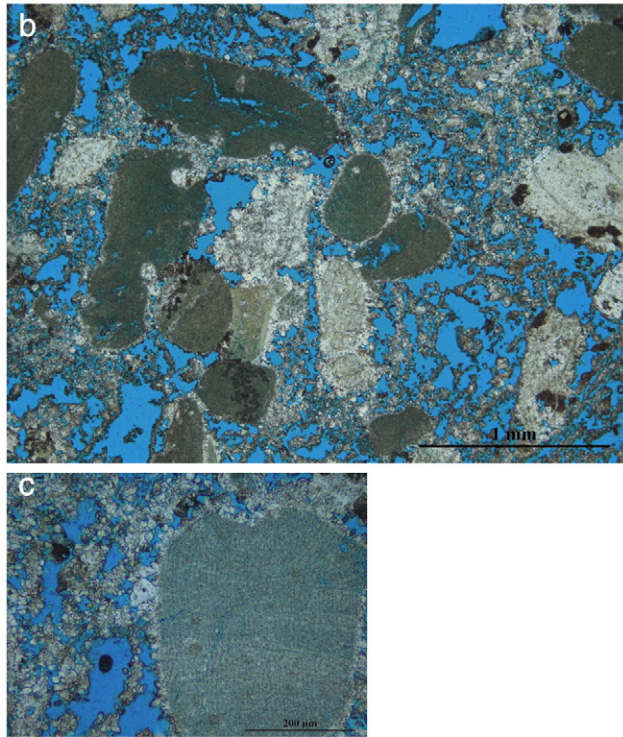
ESP Sample
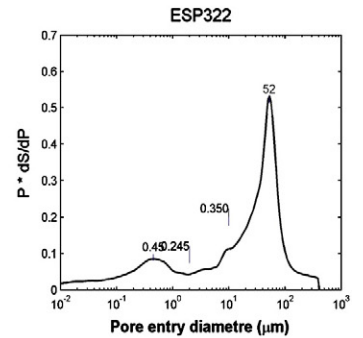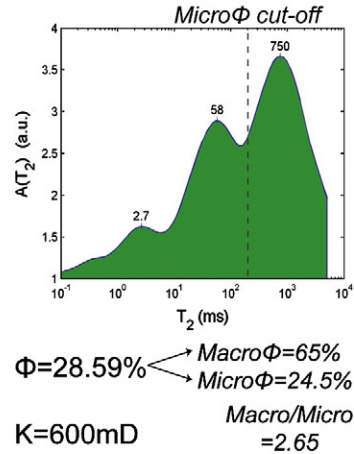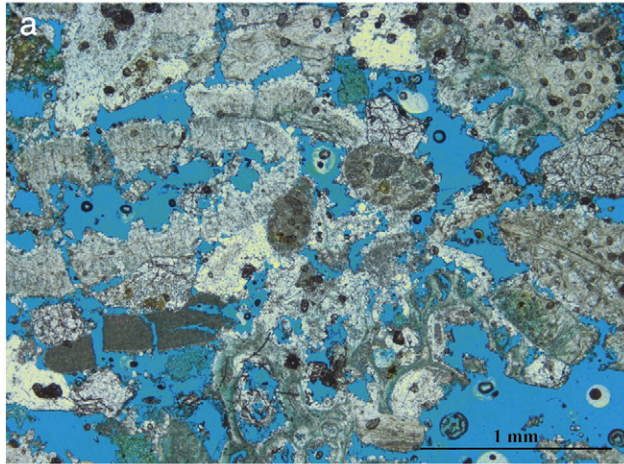
EST Sample

Fig. 12. Petrographical and petrophysical characteristics of the wide multimodal ESP and EST samples. Photo A: PL illustration of the ESP bioclastic grainstone. Remnants of a symmetrical cement rim, either with a dog-tooth or bladed fabric, can be observed around the grains; photo B: PL illustration of the EST red algae-rich grainstone. Noteworthy is the abundant thin equant circumgranular to bladed cement rim around grains; photo C: PL focus on a microporous red algae rimmed by the latter cement. In all photos, the homogeneous gray zones correspond to blue epoxy invading pore-space.

This could explain the decrease in the pore-throat-size mode of the macroporosity between EUV and EUV-HAU, i.e. respectively 64 µm and 36 µm (Figs. 6 and 11), and also the slightly higher amount of macroporosity in EUV (Table 1) than in EUV-HAU. Moreover, the microporosity contribution is higher in EUV-HAU than in EUV (Table 1).

3.4. Atypical samples

The samples from the "*Banc Royal*" Member (abbreviated BR1, 2 and 3) in the central Paris Basin are of Lutetian age. This miliolid rich grainstone characterizes agitated shoals in an inner ramp setting. The HMC of the miliolid shells is not yet stabilized, i.e. recrystallized to LMC, as illustrated by the SEM observations (Fig. 13, photo B). This has an impact

on pore space since the entire spectrum of pore sizes is represented from large intergranular macropores to very small intercrystalline micropores inside the miliolid shells (Fig. 13, photos A and B).

LAVF and LAV samples come from the *Lavoux* Limestone formation (South-West Paris Basin) of Bathonian age. LAVF is a fine ooid-peloidal grainstone with echinoderm debris, containing minor detrital micrite, and represents an inner ramp depositional environment. LAVF porosity has been partially occluded by the growth of LMC syntaxial cements on crinoidal debris (Fig. 14, photo A). Despite this phenomenon, the mesoporosity remained unplugged and/or has been created during a telogenetic alteration in the edge of the grains (Fig. 14). Intercrystalline microporosity is also present and located between the micrite crystals of both grains and the rare matrix (Fig. 14).
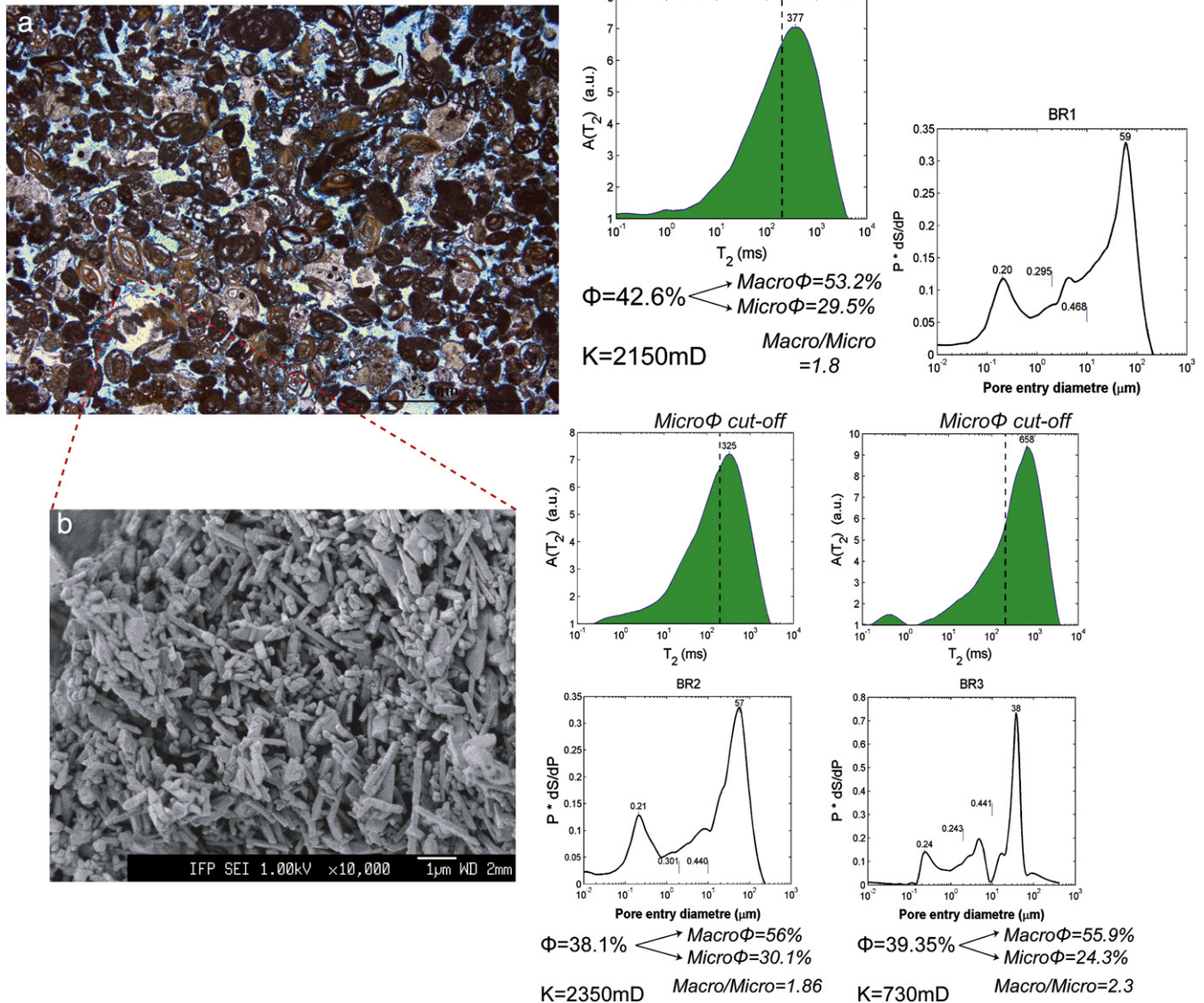
BR Samples

Fig. 13. Petrographical and petrophysical characteristics of the wide multimodal BR (1 to 3) samples. Photo A: PL illustration of the BR1 miliolid-rich grainstone; photo B: SEM view of the preserved HMC shell of the miliolid shell, explaining the low mode value of the pore throat size of the microporosity.

LAV is a clean coarse grained ooid grainstone with bivalve debris, reflecting an agitated depositional environment, in a distal inner ramp to middle ramp setting. However, the grains are heavily micritized, which is not coherent with such a depositional setting but suggests that they were originating from a more restricted/shallow environment. LAV displays a primary intergranular macroporosity, partly occluded by an equant mosaic calcite and minor planar-e dolomite crystals (Fig. 14, photo B). Partial dissolution of the calcite ooids enlarged the micropores and also created mesopores (Fig. 14).

The CHA sample comes from the *Oolithe Blanche* Limestone formation (South-East Paris Basin) of Bathonian age. It is a compacted dolomitized ooid-dominated grainstone with internal detrital micrite and small bioclasts (bivalves, echinoderm debris), which characterizes shallow-marine agitated shoals in the inner ramp. The grains are heavily micritized and are often difficult to identify clearly (Fig. 14). During burial but after a significant compaction, a sparitic calcite cement occluded most of the pore space which had locally been earlier enlarged by dissolution (ephemeral early exposures; Purser, 1978). Dolomitization is restricted to the detrital micrite. During telogenesis, undersaturated fluid partially dissolved dolomite

crystals, forming scattered rhombic moldic macropores near the location of the original interparticle pores (Fig. 14, photo C). Probably during the same time, the microporosity in the external zones of micritic and/or micritized grains was enlarged. This microporous network is continuous because of the abundant grain contacts.

This group of sample does not form a cluster in the Φ vs. K cross-plot (Fig. 7), and there is an apparent contradiction between the MICP and NMR signatures for all these samples. The NMR and MICP signatures of BR samples both indicate a continuum of sizes probably indicating a first example of pore coupling (Fig. 13). Noteworthy is the shift of the T_2 mode towards low values because of the microporosity as illustrated in BR1 and BR2 distributions, compared to BR3 which is less microporous (Fig. 13; Section 2.2). The pore-throat size modes of the microporosity of the three BR samples are very similar and restricted between 0.2 and 0.25 µm (Fig. 13). These remarkably low values are specifically related to the occurrence of microporosity inside the miliolid tests, between the HMC needle-shaped crystals (Fig. 13).

For LAV and LAVF, another pore coupling mechanism is observed, yielding a unimodal T_2 distribution while MICP distribution is bimodal (Figs. 6 and 14). A diffusional pore coupling is not easily predicted by
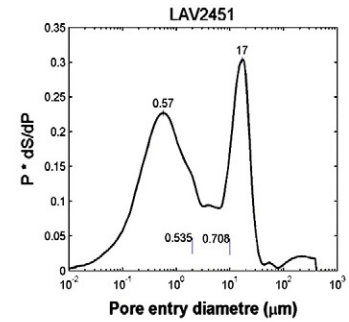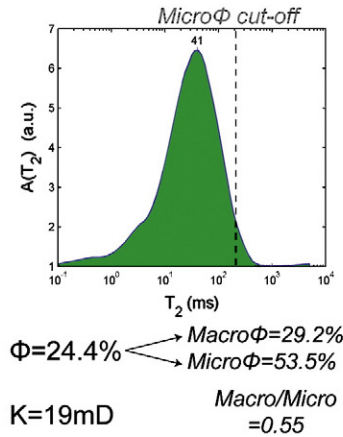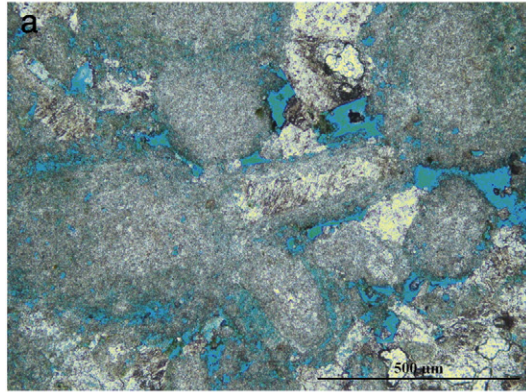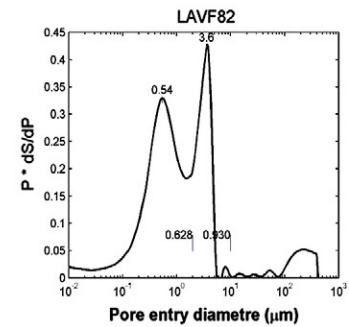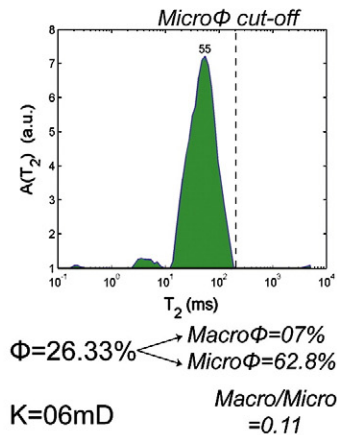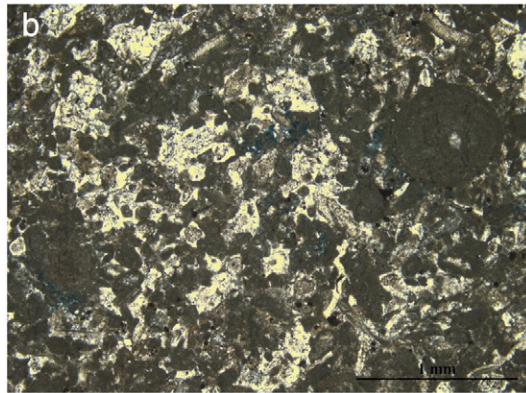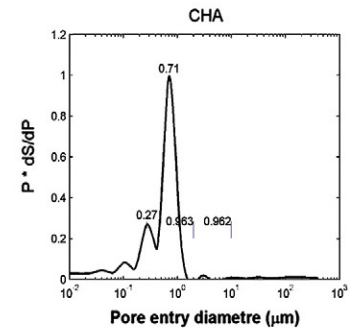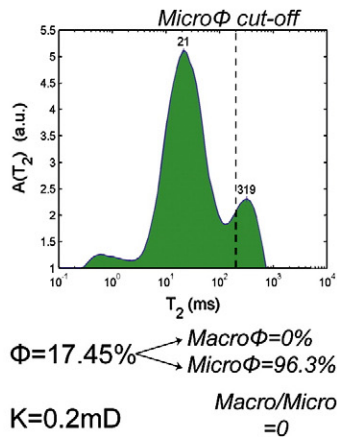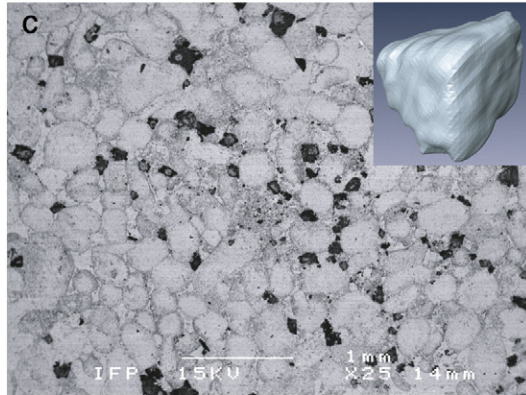
Fig. 14. Petrographical and petrophysical characteristics of the atypical samples. Photo A: PL illustration of the LAV ooid rich grainstone (homogeneous gray zones correspond to blue epoxy). Noteworthy is the spongy aspect of the micritized grains due to abundant dissolution; photo B: PL illustration of the LAVF fine ooid- and peloid-rich grainstone with internal sediment. Small (<500 μm) echinoderm debris with syntaxial overgrowths are abundant; photo C: SEM backscattered illustration of a polished epoxy impregnated CHA ooid grainstone with internal sediment. The black rhombic zones correspond to dolomite molds, also illustrated by the CT-scanner reconstruction (upper right; image width = 0.5 mm).

visual observations of the texture in thin sections, but the causes of such a phenomenon can be explained with petrography. The experimental demonstration of such coupling requires advanced NMR studies that are under progress for this sample set.

CHA has a low permeability (Fig. 7; Table 1), and a unimodal microporosity MICP signature while NMR is clearly bimodal (Figs. 6 and 14). This is because the non-percolating scattered and isolated moldic pores are accessible only through the microporosity in the micrite. The MICP only senses the pore throats of the latter (Figs. 6 and 14). On the contrary, due to the large difference in size and despite a

possible pore coupling, the NMR signature is slightly bimodal (Figs. 6 and 14).

3.5. Synthesis: consistencies and discrepancies between NMR and MICP

The NMR and MICP modal distributions of the microporous, micro–mesoporous and wide multimodal samples are consistent and even particularly similar for the microporous and wide multimodal sample sets (Fig. 6). This is not true for the atypical samples.

Diffusional pore coupling leads to a unimodal NMR T_2 distribution for BR and LAV samples despite MICP distinguishing micropores and macropores in both samples.

The decrease of the T_2 mode by the microporosity is clear when comparing BR samples to the wide multimodal samples. In fact, the T_2 mode of BR samples (300 to 700 ms) is much lower than the higher modes of the wide multimodal samples (around 1000 ms). This effect of the microporosity is even clearer for the LAV sample showing a very low T_2 mode (around 40 ms).

The CHA sample illustrates clearly the limitations of the mercury injection technique. In fact, NMR distinguishes the dolomite isolated molds from the microporous framework of the sample, whereas MICP cannot because the physical connectivity between the molds is through the microporosity (Fig. 14). The MAS sample, despite similar petrographic characteristics to the CHA samples, displays different NMR and MICP distributions (Fig. 6). First, the micrite (grains and matrix) in the CHA sample is microporous whereas this is not (or less) the case in the MAS sample (visible through the backscattered photos of both samples, respectively Figs. 10a and 14). Secondly, dolomiti-

zation is more intense in the MAS sample than the CHA sample (Figs. 10a and 14), but dedolomitization is less prominent. As a result, the pore space of the MAS sample is a continuous network of mesopores located in touching non-perfect dolomite molds, whereas the CHA pore space is most likely a continuous microporous network with isolated macro rhombic molds.

4. Discussion

The overview of this integrated petrographical and petrophysical catalog shows at least two results needing a detailed discussion: (1) the role of micritization in the homogenization of the petrophysical behavior of carbonates, and (2) the cause(s) of diffusional coupling and its impact on the interpretation of the NMR data.

Geological attributes derive from petrographic observations which are typically not quantitative, as well as potentially biased by the interpreter, and thus linking geological attributes to petrophysical properties may appear controversial. In the present paper, all the efforts were made to limit and constrain this problem. One solution to
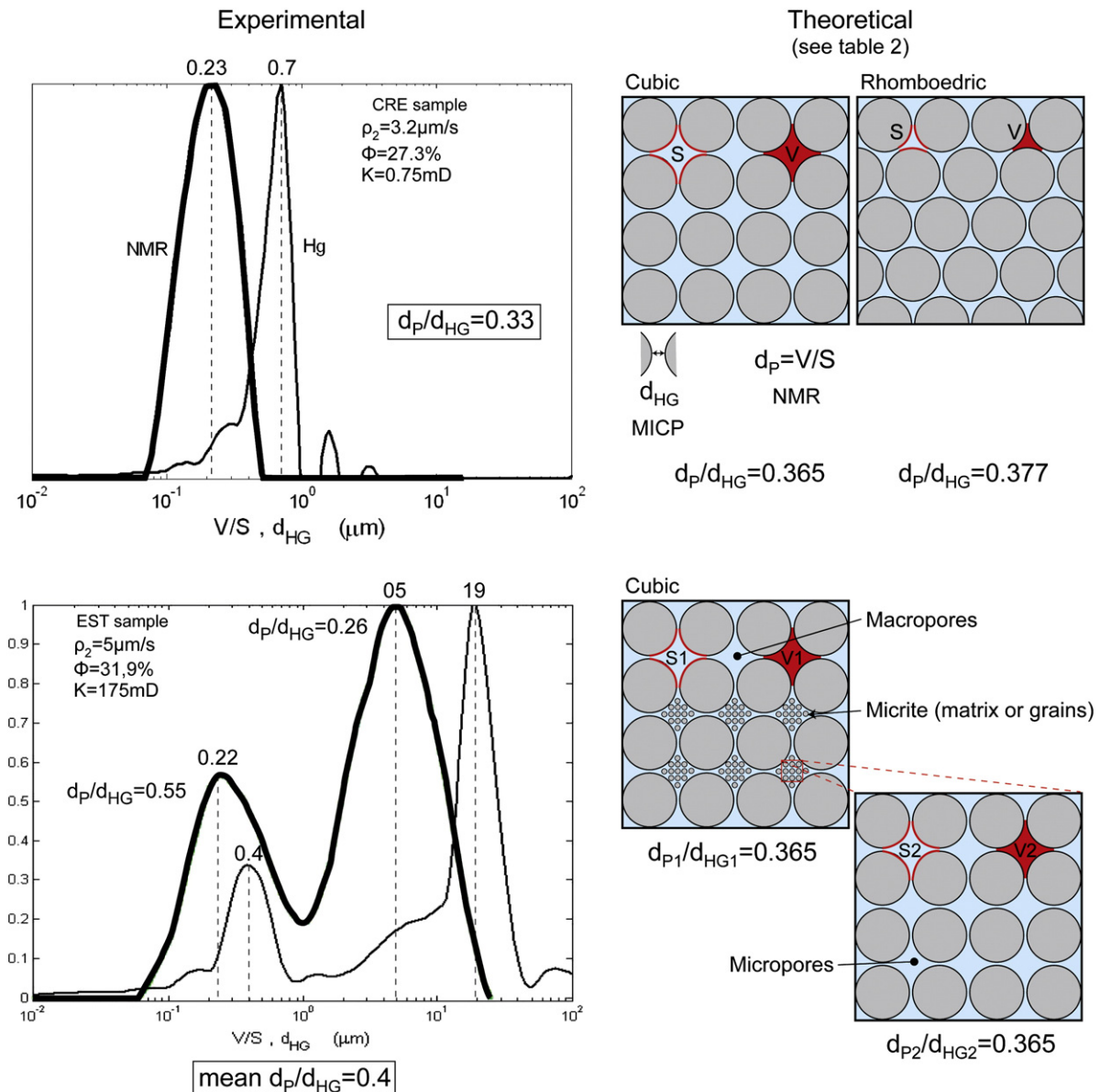

Fig. 15. Comparison between d_P (V/S, or "pore diameter") distribution, computed from the NMR T_2 distribution, and the d_{HG}, or pore-throat-size distribution, computed from MICP. Illustration from the CRE and the EST samples, respectively with unimodal and bimodal NMR/MICP distributions. The experimental d_P/d_{HG} ratios of both samples are close from the theoretical sphere packing model (cubic or rhomboedric) ratios. This is especially true for the microporous unimodal CRE sample.

improve on this would be, for instance, the use of high resolution CT imagery and co-registered SEM as petrographic calibrating parameters, even if such an approach still gets a limiting resolution, in particular with respect to micro/meso- and nanoporosity.

4.1. Impact of micritization on the pore-space

With the help of the specific surface area measurements, it is possible to convert the NMR T_2 distribution into a distribution of V/S, i.e. a length scale d_p, characterizing pores in the sample (Fig. 15) and compare d_p with the dimension of the throats to access the pores. As explained in Section 2.2 and Table 2, in a sphere packing model, either cubic or rhomboedric, d_p is approximately 3 times lower than d_{HG}. Noteworthy is the behavior of the microporous samples displaying d_p/d_{HG} ratios close to the theoretical sphere packing model ratios (0.33 for the CRE samples compared to the theoretical 0.365 and 0.377; Fig. 15). This means that in these samples, the natural organization of the microcrystalline calcite

rhombic crystals (1 to 5 μm; Fig. 9a, b, c) constituting the micrite displays a sphere packing configuration (Fig. 15).

The petrophysical properties of the grainy GUD and ANS carbonates are similar, and are both comparable to the fine CRE carbonate due to micritization of their constitutive grains. Despite GUD and ANS reflecting more complex depositional facies, their pore network could be also simplistically considered as the space located in between a packing of microspheres, i.e. the microcrystalline calcite crystals. The connectivity of such a network is obvious for the homogeneous CRE micrite (Fig. 16, photos A and B), but not for the two other carbonates. In fact, the density and the close packing of polymodal grains constituting the GUD sample, and the local occurrence of an intergranular micrite matrix where the grains are less abundant explain the connectivity of the pore network (Fig. 16, photos C and D). For the ANS sample, the absence of an early cement rim around grains (Fig. 9c) did not prevent mechanical compaction during burial as illustrated by the numerous imbricate grains, spalled
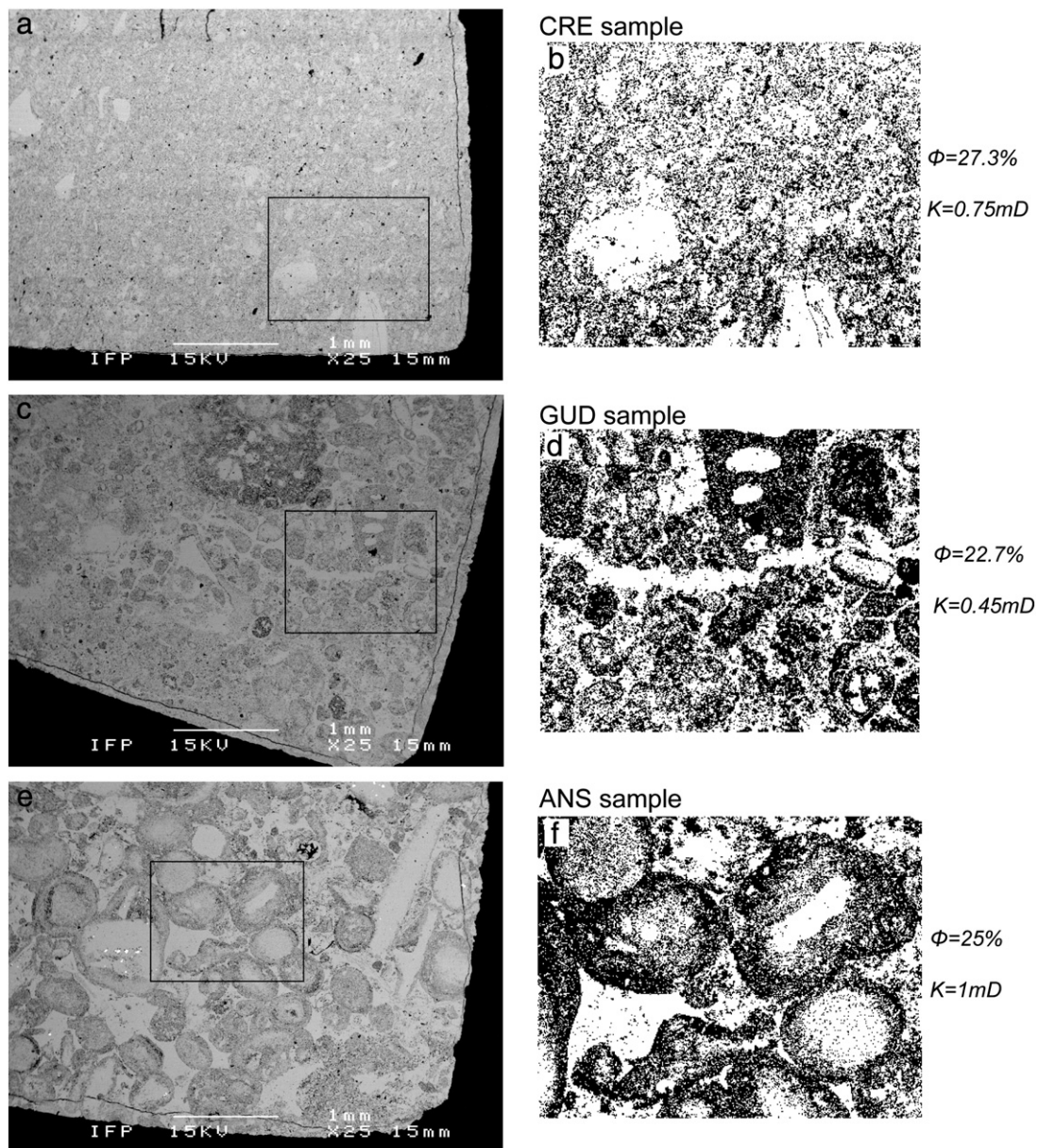

Fig. 16. Illustration of the connectivity of the microporous network for the 3 microporous samples. Photos A, C, and E: SEM backscattered large photo of polished epoxy impregnated slabs of CRE, GUD, and ANS samples respectively. Photos B, D, and F: gray level focus images treated with threshold levels (identical in all 3 samples) to emphasize the porous zones (black). The connectivity is obvious for CRE but also clearly demonstrated for GUD and ANS.

ooids, or even microstylolites (Figs. 9c and 16). Despite the rare occurrence of a micritic matrix, the contacts between the micritized grains are so numerous that the microporous network is continuous (Fig. 16, photos E and F). The ANS sample can be considered as a skeleton of microporous spongy grains maintained by a solid equant mosaic calcite cement framework. This description is applicable to most of the ooid dominated limestone formations of Bathonian age in the Paris Basin, which are today considered as potential targets for CO_2 storage (Casteleyn et al., 2010; Rigollet et al., 2007).

Micritization, a common early diagenetic process in low energy carbonate lagoonal environments (Bathurst, 1971), has an indirect impact on the petrophysical properties of carbonate rocks, but is often neglected or underestimated. In this sample data set the reservoir properties are only moderately modified, since microporosity was moderately enlarged through telogenetic dissolution (micropores lower than 05 μm) and has little influence on permeability (Melim et al., 2001; i.e. high porosity >20% and low permeability ≈ 1 mD). But in the subsurface later – younger – diagenetic events like deep burial corrosion can significantly alter and enhance the petrophysical properties and, as a consequence, understanding micritization and later dissolution is critical for the understanding of reservoir quality in gas reservoirs or fractured oil reservoirs (e.g. Lambert et al., 2006).

4.2. NMR diffusional coupling

Several, so-called atypical, samples display d_p/d_{HG} ratios similar to the microporous samples. The EST sample is characterized by bimodal MICP and NMR distributions (Fig. 12). It is surprising to see that d_p/d_{HG} ratios of both intergranular macropores (0.26) and, to a lesser degree, intragranular micropores (0.55) deviate not too much from the theoretical sphere packing model ratios (Fig. 15). Here the arrangement of the various bioclasts mimics a "macro"sphere packing arrangement, while the arrangement of the microcrystalline calcite crystals (1 to 5 μm; Fig. 9a, b, c), constituting the microporous red algae, is not so far from a "micro"sphere packing arrangement. The two different pore networks are here weakly coupled by diffusion and a clear bimodal T_2 distribution is observed because of the occurrence of an early thin equant circumgranular to bladed isopachous cement rim around the grains (Fig. 12, photos B and C). It is continuous enough to isolate the molecular motions in the intragranular micropore network of the red algae from that of the intergranular macropore network. Water molecules therefore separately explore by diffusion both pore spaces during the magnetization decay (Fig. 17). The local porosity of that cement rim governs the diffusion exchange and may be small. However, there are definitely some physical connections between micro and macropores since (1) water saturation for NMR analysis is complete, and (2) MICP clearly illustrates two classes of pores (Figs. 12 and 17).

The LAV ooid and bioclastic grainstone are petrographically rather similar to the EST bioclastic grainstone (Fig. 17, photos A and C), and both display a bimodal MICP pore-throat-size distribution (Fig. 17). However, the LAV NMR T_2 distribution is unimodal whereas the EST one is bimodal (Fig. 17). Thus a comparison with the theoretical sphere packing arrangement is impossible for LAV. This difference lies in the absence of an isopachous early cement rim in the LAV sample. As a consequence the intragranular micropore network of the micritized ooids is not isolated from the intergranular macropore network. Water molecules uniformly explore by diffusion both pore spaces during the magnetization decay (Fig. 17).

With the exception of BR1, the NMR patterns of the wide multimodal samples closely reflect the MICP patterns and do not display any diffusional coupling effect. EUV and EUV-HAU samples display syntaxial overgrowths on crinoid ossicles which play the same role as the isopachous early cement rim of EST sample. This is, however, less obvious for the ESP sample where the remnants of

isopachous cement rims probably do not completely isolate the intragranular and intergranular pore systems.

Early cement rims have a direct antagonistic impact on the reservoir properties of grainy carbonates since they can reduce the pore space as well as prevent or hamper mechanical and even chemical compaction (e.g. Melzer and Budd, 2008; Moore, 2002). But such cements can also strongly impact the NMR response of similar carbonates (similar MICP signature, Φ, etc.), which is of major importance for considering the NMR tool for rock-typing purposes.

In addition, the pore-coupling phenomenon directly impacts the T_2 log mean average of the T_2 distribution which is a key parameter for calculating the permeability from the NMR log data by the use of the SDR (Schlumberger-Doll-Research) equation (Kenyon et al., 1986). Since the pore-coupling phenomenon modifies the shape of the T_2 distribution, it also impacts the position of the cut-off defining the free fluid volume (BVM or Bulk Volume Movable) and bound fluid volume (BVI or Bulk Volume Irreducible), necessary for calculating the permeability with the Timur–Coates equation (e.g. Frank et al., 2005; Westphal et al., 2005).

Finally, a key point is that physical connectivity, illustrated by MICP experiments, and diffusional pore coupling are not linked together.

5. Conclusions

On the basis of 16 natural outcrop samples, covering a wide range of both the sedimentary facies occurring on carbonate platform systems, and the petrophysical properties, this study provides ideas and insights to both sedimentologists and petrophysicists when interpreting NMR and MICP analyses.

MICP and petrographic investigations allowed the samples to be split into four main groups, namely: microporous samples, micro–mesoporous samples, wide multimodal samples, and atypical samples. Based on the microporous sample set a NMR microporosity threshold is defined at a T_2 of 200 ms.

Completely different sedimentary facies, for instance micritized grainstone and homogeneous mudstone/wackestone, can display identical NMR and MICP signals (and also similar porosity and permeability) as demonstrated by the microporous sample set. This is not new but emphasizes the role of the micritization of grains, an underestimated although frequent process, in the evolution of petrophysical properties of carbonates. Mudstone/wackestone and heavily micritized grainstone display similar behavior as a theoretical sphere packing model. NMR together with MICP provide detailed insights into the pore network independently from the depositional facies.

In contrast, petrographically similar sedimentary facies with identical MICP curves, related to similar depositional environments, for instance macroporous bioclastic and ooid grainstones, can display completely different NMR signals. The modeled diffusional pore coupling phenomenon, i.e. the diffusion of water molecules between intragranular micropores and intergranular macropores during the magnetization decay, is clearly illustrated in non early cemented grainstones. In this case, the NMR signal is unimodal and shifts to microporosity T_2 values. When continuous early cement rims and/or syntaxial overgrowths developed around grains, the diffusional pore coupling phenomenon may not occur due to the isolation of pore spaces and the NMR signal may therefore be bimodal. This is of importance for those who aim to use the NMR in the rock-typing of carbonates, since NMR is then a complementary tool to MICP which does not illustrate alone the reality of the pore-space. But the pore-coupling phenomenon potentially strongly disturbs the permeability calculations from NMR data through its impact on the shape of the T_2 distribution. This result also displays again the influence of early diagenetic cementation on carbonate petrophysics.
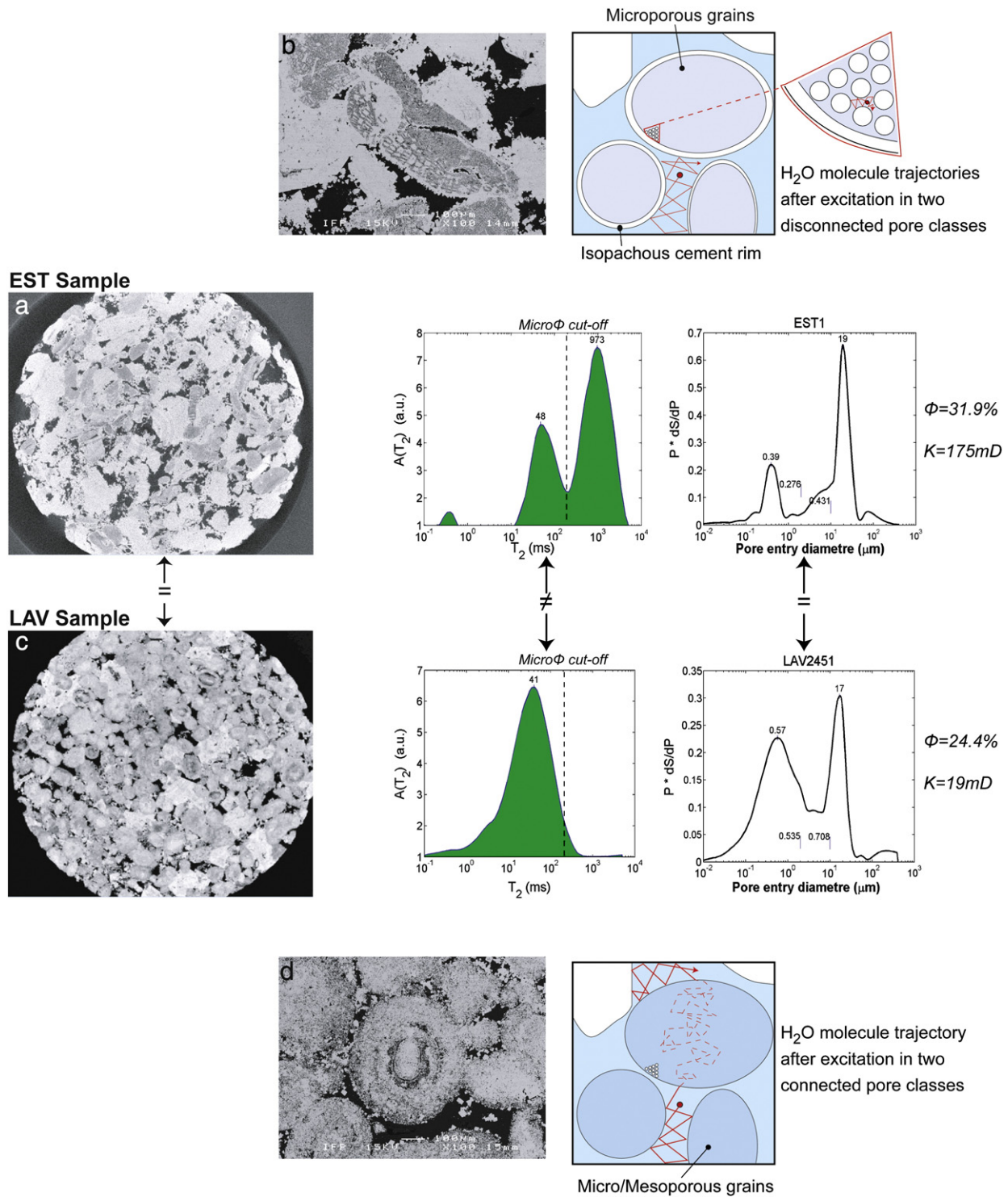
Fig. 17. Comparison between 2 petrographically similar samples (EST and LAV). They display similar MICP but distinct NMR signals. Photos A and C: 2D CT scanner image of plugs. Photos B and D: SEM backscattered focus images of polished epoxy impregnated slabs (porosity is black). The difference between the NMR T_2 distributions is explained by a diffusional pore coupling effect: for EST, water molecules explore separately by diffusion of both the macroporous and the microporous networks during the magnetization decay, whereas for LAV, water molecules uniformly explore both pore spaces during the magnetization decay (see further explanations in the text).

More generally, this study clearly demonstrates that NMR is a powerful complementary tool to MICP for the analysis of pore networks in carbonates. The particular interest of NMR compared to MICP is its application as a logging tool. However, and as already demonstrated by Westphal et al. (2005), a genetic geological knowledge remains necessary to interpret NMR data.

References

Akbar, M., Petricola, M., Watfa, M., Badri, M., Charara, M., Boyd, A., Cassel, B., Nurm, I.R., Delhomme, J.-P., Grace, M., Kenyon, B., Roestenburg, J., 1995. Classic interpretation problems: evaluating carbonates. Oilfield Rev. 7 (1), 38–57.

Akbar, M., Vissapragada, B., Alghamdi, A.H., Allen, D., Herron, M., Carnegie, A., Dutta, D., Olesen, J.M., Chourasya, M.D., Logan, D., Stief, D., Netherwood, R., Duffy Russel, F., Saxena, K., 2001. A snapshot of carbonate reservoir evaluation. Oilfield Rev. 20–41.

Allen, D.F., Boyd, A., Massey, J., Fordham, E.J., Amabeoku, M.O., Kenyon, W.E., Bard, W.B., 2001. The practical application of NMR logging in carbonates: 3 case studies. Proceeding of the SPWLA 42nd Annual Symposium. June 17–20.

Anand, V., Hirasaki, G.J., 2005. Diffusional coupling between micro and macroporosity for NMR relaxation in sandstones and grainstones. Proceedings of SPWLA 46th Annual Logging Symposium, New Orleans, LA.

Bathurst, R.G.C., 1971. Carbonate sediments and their diagenesis. Developments in Sedimentology, 12. 620 pp.

Bousquie, P., 1979. Texture and porosity of carbonate rocks. Ph.D. thesis, Paris VI University.

Brunauer, S., Emmett, P.H., Teller, E., 1938. Adsorption of gases in multimolecular layers. J. Am. Chem. Soc. 60 309 pp.

Burchette, T.P., Wright, V.P., 1992. Carbonate ramp depositional systems. Sed. Geol. 79, 03–57.

Casteleyn, L., Robion, P., Collin, P.Y., Menendez, B., David, C., Desaubliaux, G., Fernandes, N., Dreux, R., Badiner, G., Brosse, E., Rigollet, C., 2010. Interrelations of the petrophysical, sedimentological and microstructural properties of the Oolithe Blanche Formation (Bathonian, saline aquifer of the Paris Basin). Sediment. Geol. doi:10.1016/J.sedgeo.2010.07.003.

Choquette, P.W., Pray, L.C., 1970. Geologic nomenclature of porosity in sedimentary carbonates. AAPG Bull. 54 (2), 207–250.

Choquette, P.W., Pray, L.C., 1972. Geologic nomenclature and classification of porosity in sedimentary carbonates. Carbonate Rocks II: Porosity and Classification of Reservoir Rocks: AAPG Repr. Ser., 5, pp. 154–197.

Combarnous, M., Marle, C., 1965. Méthodes d'études de la texture des solides poreux. Génie Chim. 94 (2) (in French).

Dennis, B., 1997. Pores explored. Middle East Well Eval. Rev. 19, 03–65.

Dullien, 1992. Porous Media, Fluid Transport and Pore Structure. Academic Press.

Dunham, R.J., 1962. Classification of carbonate rocks according to depositional texture. In: Ham, W.E. (Ed.), Classification of Carbonate Rocks: AAPG Mem., 1, pp. 108–121.

Dunn, K.J., Bergmann, D.J., Latorraca, G.A., 2002. Nuclear Magnetic Resonance; petrophysical and logging applications. Handbook of Geophysical Exploration, Pargamon.

Enay, R., Boullier, A., 1981. L'âge du complexe récifal des côtes de Meuse entre Verdun et Commercy et la stratigraphie de l'Oxfordien dans l'Est du Bassin de Paris. Geobios 14, 727–771 (in French).

Fleury, M., 2000. The use of NMR in petrophysics: from physical principles to applications. DiaLog 8 (3) 2 pp. (online).

Fleury, M., Soualem, J., 2009. Quantitative analysis of diffusional pore coupling from T2-store–T2 NMR experiments. J. Colloid Interface Sci. 336, 250–259.

Fleury, M., Santerre, Y., Vincent, B., 2007. Carbonate rock typing from NMR relaxation measurements. Proceedings of SPWLA 48th Annual Meeting, Austin, Texas. June 3–6.

Flugel, E., 2004. Microfacies Analysis of Limestones, 2nd ed. Springer-Verlag. 633 pp.

Folk, R.L., 1959. Practical petrographic classification of limestones. AAPG Bull. 43, 01–38.

Frank, S., Narayanan, R., Hansen, P.M., Allen, D., Albrechtseen, T., Steinhardt, H., Raven, M., Fordham, E., Bize, E., Rose, D., 2005. Carbonate rock typing using NMR data: a case study from Al Shaheen field, offshore Qatar. International Petroleum Technology Conference, Doha. 21–23 November.

Godefroy, S., Korb, J.-P., Fleury, M., Bryant, R.G., 2001. Surface nuclear magnetic relaxation and dynamics of water and oil in macroporous media. Phys. Rev. E 64.

Goni, I., Ragot, J.P., Sima, A., 1968. Méthode d'étude du champ microfissural des minéraux et des roches et possibilités d'applications en géologie. Bull. BRGM, n°4, pp. 51–92 (2nd series), section II, (in French).

Gregg, J.M., Sibley, D.F., 1984. Epigenetic dolomitization, the origin of xenotopic dolomite texture. J. Sediment. Petrol. 54, 907–931.

Kenter, J.A.M., Anselmetti, F.S., Kramer, P.H., Westphal, H., Vandamme, M.G.M., 2002. Acoustic properties of "young" carbonate rocks, ODP Leg 166 and boreholes Clino and Unda, Western Great Bahama bank. J. Sediment. Res. 72 (1), 129–137.

Kenyon, W.E., Day, P.I., Straley, C., Willemsen, J.F., 1986. A three-part study of NMR longitudinal relaxation studies of water saturated sandstones. SPE Formation Evaluation. September, 662–636.

Lambert, L., Durlet, C., Loreau, J.P., Marnier, G., 2006. Burial dissolution of micrite in Middle East carbonate reservoirs (Jurassic–Cretaceous): keys for recognition and timing. Mar. Petrol. Geol. 23, 79–92.

Lenormand, R., 2003. Interpretation of mercury injection curves to derive pore size distribution. Proceeding of SCA Annual conference.

Lindholm, R.C., Finkelman, R.B., 1972. Calcite staining: semiquantitative determination of ferrous iron. J. Sediment. Petrol. 42, 239–242.

Lønøy, A., 2006. Making sense of carbonate pore system. AAPG Bull. 90 (9), 1381–1405.

Lucia, J.L., 1999. Carbonate Reservoir Characterization. Springer-Verlag. 226 pp.

Melim, L.A., Anselmetti, F.S., Eberli, G.P., 2001. The importance of pore type on permeability of Neogene carbonates, Great Bahama Bank. In: Ginsburg, R.N. (Ed.), Subsurface Geology of a Prograding Carbonate Platform Margin, Great Bahama Banks: SEPM Spec Publ., 70, pp. 217–240.

Melzer, S., Budd, D.A., 2008. Retention of high permeability during shallow burial (300 m to 500 m) of carbonate grainstones. J. Sed. Res. 78, 548–561.

Minh, C.C., Petricola, M., Dennis, B., 1997. The carbonate challenge. Middle East Well Eval. Rev. 20, 36–55.

Moore, C.H., 2002. Carbonate diagenesis and porosity. Developments in Sedimentology, 46. Elsevier, Amsterdam. 338 pp.

Moss, A.K., 2000. The ART NMR carbonate rock catalogue: a library of NMR response characteristics in carbonate rocks. DiaLog 8 (3) (online).

Nurmi, R., Standen, E., 1997. Carbonates, the inside story. Middle East Eval. Rev. 18, 28–41.

Pittman, E.D., 1971. Microporosity in carbonate rocks. AAPG Bull. 55 (10), 1873–1881.

Purser, B.H., 1978. Early diagenesis and the preservation of porosity in Jurassic limestones. J. Petrol. Geol. 1 (2), 83–94.

Reading, H.G., 1996. Sedimentary Environments: Processes, Facies, and Stratigraphy, Third edition. Blackwell Science Ltd. 688 pp.

Rigollet, C., Collin, P.Y., Badinier, G., Brosse, E., 2007. CO2 geological storage in France (Dogger, Paris Basin) in depleted reservoirs and aquifers — sedimentologist inputs. ASF Meeting, French Sedimentological Congress 2007, Caen.

Skalinski, M., Kenter, J., Jenkins, S., 2009. Rock type definition and pore type classification of a carbonate platform, Tengiz field, Republic of Kazakhstan. Proceedings of SPWLA 50th Annual Meeting. June 21–24.

Toumelin, E., Torres-Verdin, C., Chen, S., 2003. Modeling of multiple echo-time NMR measurements for complex pore geometries and multiphase saturations. SPE Annual Technical Conference and Exhibition, SEP 29–OCT 02, 2002 San Antonio, Texas: Spe Reservoir Evaluation & Engineering, Vol. 6, pp. 234–243. Iss. 4.

Vincent, B., 2001. Sédimentologie et Géochimie de la diagenèse des carbonates. Application au Malm de la bordure Est du Bassin de Paris. PhD Thesis, University of Burgundy, 380p (in French).

Vincent, B., Emmanuel, L., Houel, P., Loreau, J.P., 2007. Geodynamic control on carbonate diagenesis: petrographic and isotopic investigation of the Upper Jurassic formations of the Paris Basin (France). Sed. Geol. 197, 267–289. doi:10.1016/j.sedgeo.2006.10.2008.

Westphal, H., Surholt, I., Kiesl, C., Thern, H.F., Kruspe, T., 2005. NMR measurements in carbonate rocks: problems and an approach to a solution. Pure Appl. Geophys. 162, 549–570.

Zinszner, B., Pellerin, F.M., 2007. A Geoscientist's Guide to Petrophysics, Technip editions. IFP Publications. 384 pp.